The solubility of $ErPO_4$ and Er speciation in hydrothermal fluids at varying pH and salinity between 350 and 450 °C

CHARLES T. KERSHAW[1*], NICOLE C. HURTIG[1], ALEXANDER P. GYSI[1,2], ARTAS A. MIGDISOV[3], LAURA E. WATERS[1], DANIEL HARLOV[4,5,6]

[1] Department of Earth and Environmental Science, New Mexico Tech, Socorro, New Mexico 87801, USA

[2] New Mexico Bureau of Geology and Mineral Resources, New Mexico Tech, Socorro, New Mexico 87801, USA

[3] Earth and Environmental Division, Los Alamos National Laboratory, Los Alamos, NM 87545, USA

[4] Deutsches GeoForschungsZentrum GFZ, Telegrafenberg, 14473 Potsdam, Germany

[5]Faculty of Earth Resources, China University of Geosciences, Wuhan 430074, China

[6]Department of Geology, University of Johannesburg P.O. Box 524, Auckland Park, 2006 South Africa

*Corresponding author: charles.kershaw@student.nmt.edu

Corresponding author: charles.kershaw@student.nmt.edu

REVISION 1

Submitted to GCA: *Accepted*

Keywords: *Aqueous Er speciation, Solubility of $ErPO_4$, Experiments, Thermodynamics*

23

24

25

26

Abstract

The rare earth elements (REE) are important for the green-energy transition and can be incorporated into the REE phosphates, such as xenotime-(Y), which also hosts heavy REE (Tb–Lu). Xenotime-(Y) is a common accessory mineral in metamorphic rocks and a range of mineral deposits where it controls the mobility of heavy REE, however, the impact of high temperature aqueous fluids on the behavior of heavy REE is largely unknown. Thermodynamic modeling can be utilized as a tool to predict the mobility of REE in hydrothermal aqueous fluids, but must be supported by accurate experimental data. Here, we measured the solubility of endmember synthetic xenotime-structured $ErPO_4$ in NaCl-HCl-NaOH-bearing aqueous solutions at 350 °C and water vapor saturation pressure, at 400 and at 450 °C and 500 bar using batch-type Inconel reactors. Erbium speciation was investigated as a function of pH from 2.8 to 8, where Er chloride species are predominant at acidic conditions (pH <3) and Er hydroxyl complexes are predominant at near-neutral to alkaline conditions (pH >3). At pH 7–9, the measured $ErPO_4$ solubility (-9.8 to -7.5 log m_{Er}) is up to 2.5 orders of magnitude lower than thermodynamic predictions (-9.4 to -6.7 log m_{Er}) using existing thermodynamic databases. At pH 2–3, the predicted $ErPO_4$ solubility is ~0.5 orders of magnitude higher at 350 °C and ~1 order of magnitude lower at 450 °C compared to experimentally measured Er concentrations. The thermodynamic properties of aqueous Er species were therefore revised in this study. The partial molal Gibbs energy of formation ($\Delta_f G^0_{T,P}$) for aqueous Er hydroxyl and chloride species are optimized using GEMSFITS and the logarithmic formation constants ($\log\beta_n^{(Cl,OH)}$) were derived at each experimental temperature and pressure:

T	P	$\log\beta_1^{OH}$	$\log\beta_2^{OH}$	$\log\beta_3^{OH}$	$\log\beta_1^{Cl}$	$\log\beta_2^{Cl}$

(°C)	(bar)					
350	165	9.16	19.03	21.53	2.63	5.02
400	500	10.99	22.12	27.9	5.88	7.8
450	500	16.04	28.9	40.19	8.13	17.75

The updated thermodynamic properties for Er hydroxyl species ($Er(OH)^{+2}$, $Er(OH)_2^{+}$, and $Er(OH)_3^{0}$) show that their stability shifts to more acidic conditions at and below 400 °C. The Er chloride species ($ErCl^{+2}$ and $ErCl_2^{+}$) show increased stability compared to Er hydroxyl species at temperatures of 450 °C and 0.01 mol/kg NaCl. The updated thermodynamic properties are implemented into the GEM-Selektor modeling package to investigate the mobility of Er in saline hydrothermal fluids in equilibrium with alkaline rocks. Importantly, the updated properties for Er hydroxyl species result in low Er solubility at rock equilibrated pH conditions due to an expanded hydroxyl predominance zone, but lower aqueous complex stability overall, whereas previous models suggest greater stability for aqueous Er species. Furthermore, $ErPO_4$ solubility increases with decreasing temperature due to the deprotonation of HCl, which increases the acidity of hydrothermal fluids and the availability of Cl^- to complex with the REE. These simulations highlight how fluid-rock reaction and temperature affect the mobility of REE in hydrothermal ore-forming systems.

1. INTRODUCTION

Erbium is a member of the heavy rare earth elements (HREE) including Tb to Lu and Y, which are characterized by their comparatively smaller ionic radii and paired 4*f* electron orbitals within the ‘lanthanide contraction’ series. Erbium is an important element used in YAG lasers, as red and

green phosphors, and in fiber-optic cables (Haque et al., 2014; Jowitt, 2022). The rare earth elements (REE) are mined from magmatic-hydrothermal ore deposits including carbonatites, peralkaline and alkaline igneous complexes, and iron oxide apatite deposits. Ore formation commonly involves a combination of magmatic and hydrothermal processes, where REE are initially fractionated and enriched through magmatic processes (i.e., partial melting, fractional crystallization, and/or melt immiscibility), and then are subsequently mobilized by hydrothermal fluids and precipitated in veins and breccias. Hydrothermal processes are crucial in reaching sufficient enrichment of REE to make extraction economic and can be observed in deposits such as Bayan Obo in China, Bear Lodge in USA, Pea Ridge in USA, and Strange Lake in Canada (Smith et al., 1999; Williams-Jones et al., 2012; Moore et al., 2015; Andersen et al., 2016; Gysi et al., 2016; Hofstra et al., 2016; Harlov et al., 2016). Therefore, understanding the behavior of REE in high temperature hydrothermal fluids has become paramount for predicting REE mobility and understanding their enrichment processes in geological systems.

Mobilization and concentration of REE in hydrothermal fluids is controlled by the stability of the aqueous complexes and the solubility of REE-bearing minerals (Wood, 1990; Williams-Jones et al., 2012; Gysi et al., 2016; Migdisov et al., 2016; Di and Ding, 2024). In acidic Cl-bearing hydrothermal fluids, Er chloride species are predicted to control Er mobility, whereas in more alkaline fluids Er hydroxyl species predominate (Wood, 1990; Gammons et al., 2002; Migdisov et al., 2009, 2016; Gysi et al., 2015; Perry and Gysi, 2018). Solubility experiments in acidic perchlorate-bearing fluids at 100–250 °C indicate control of $ErPO_4$ solubility by the Er^{+3} aqua ion at low pH (Gysi et al. 2015). In NaCl-HCl-bearing solutions at acidic conditions, the $ErCl^{+2}$ and $ErCl_2^+$ species predominate at 150–250 °C (Migdisov et al., 2009). *In situ* UV-vis spectroscopic studies indicate that Er chloride species become predominant over Er^{+3} above 150 °C in Cl-rich

fluids (Migdisov and Williams-Jones, 2006) and Er hydroxyl species predominate at alkaline conditions in Cl-free solutions at 25 °C (Han and Gysi, 2024, 2025). High-energy X-ray scattering (HEXS) has been used to provide formation constants at ambient temperatures for $ErCl^{+2}$ and $ErCl_2^+$ in concentrated (4 mol/kg) electrolyte solutions (Soderholm et al., 2009). The latter are lower than those reported in Migdisov et al. (2009) but are comparable to those in the model by Haas et al. (1995). Erbium behavior in Cl-bearing solutions has also been explored using extended X-ray absorption fine structure (Bera et al., 2015) and Raman spectroscopy (Rudolph and Irmer, 2019). Erbium hydroxyl speciation has been measured experimentally from 25–75 °C by Han and Gysi (2024, 2025), who derived the hydrolysis constants for $Er(OH)^{+2}$, $Er(OH)_2^+$, and $Er(OH)_3^0$.

Thermodynamic properties for aqueous REE species derived by Haas et al. (1995) are based on low temperature experimental data (25 °C and 1 bar) from Smith and Martell (1976) and Lee and Byrne (1992). Thermodynamic properties were extrapolated using the Helgeson-Kirkham-Flowers (HKF) equation-of-state (Helgeson et al., 1981; Shock et al., 1992; Shock and Helgeson, 1988; Tanger and Helgeson, 1988) to model REE speciation up to 1000 °C and 5000 bar, with the HKF parameters and constants originally compiled in the program SUPCRT92 (slop98.dat; Johnson et al., 1992). Comparison of predicted thermodynamic properties from Haas et al. (1995) with experimental results have revealed significant discrepancies for Er species even at temperatures up to 250 °C (Gammons et al., 2002; Migdisov and Williams-Jones, 2006; Migdisov et al., 2009; Gysi et al., 2015; Han and Gysi, 2024; Pan et al., 2024). Pan et al. (2024) recently optimized Er^{+3} and Er hydroxyl species using $REEPO_4$ solubility experimental data in Cl-free solutions up to 300 °C (Gysi et al., 2015). The thermodynamic properties of $ErCl^{+2}$ and $ErCl_2^+$ were updated based on UV-Vis spectrophotometry experiments by Migdisov and Williams-Jones (2006) and solubility data by Migdisov et al. (2009) up to 250 °C. However, since no experimental

data exists above 300 °C for Er-chloride or hydroxyl species, the accuracy of predicted REE speciation and mobility remains untested in high temperature fluids.

In this study, we investigate the solubility of $ErPO_4$ in Cl-bearing solutions at 350 °C and water vapor saturation pressure, P_{sat}, and at 400 and 450 °C and 500 bar using batch-type Inconel reactors. Erbium speciation is derived from slope relationships as a function of logarithmic Er molality with varying starting pH (2, 3, 4, and ~10) and logarithmic chloride concentration (0.01, 0.1 and 0.5 mol/kg NaCl). Erbium chloride ($ErCl^{+2}$, $ErCl_2^{+}$) and hydroxyl species ($Er(OH)^{+2}$, $Er(OH)_2^{+}$, $Er(OH)_3^{0}$) are optimized using GEMSFITS (Miron et al., 2015) based on experimental data in this study. The optimized thermodynamic properties for Er species were implemented into the GEM-Selektor software package and combined with minerals and other aqueous and gaseous species from the MINES thermodynamic database to model the solubility of $ErPO_4$ for a case study of the Strange Lake pegmatite (Canada). The simulated fluid-rock systems provide valuable insights into the role of chloride and hydroxyl ligands for the mobilization of HREE in granite associated fluids.

2. METHODS

2.1. Materials

Experimental starting solutions with different starting pH of 2, 3 and 4 were prepared at ambient (22 ±2°C) temperature using Milli-Q water (18 MΩ·cm) and variable amounts 0.09990 ±0.00054 mol/l HCl standard solution (Inorganic Ventures). After measuring the pH of these solutions, NaCl powder (Thermo Scientific >99.0% trace metal grade) was added to an aliquot of these solutions to make a 0.5 mol/kg solution at each pH. The 0.5 m NaCl solutions were subsequently diluted at

their respective pH for both the 0.1 and 0.01 mol/kg NaCl solutions. The alkaline solution with a starting pH of 10 ±0.5, was prepared by making the NaCl solutions first and adding a small aliquot of 1:10 diluted 0.09988 ±0.00039 mol/l NaOH standard solution (Inorganic Ventures) on the day of the experiment. The alkaline solutions were made fresh on the day of the experiment and purged with N_2 gas (Airgas research grade) to remove atmospheric O_2 and CO_2. This process is important for mitigating shifts in pH that can occur if alkaline solutions are not fresh. The pH values of the experimental solutions were measured regularly and are within the analytical uncertainty of the pH electrode (±0.02). The Na concentration of the experimental solutions was measured using inductively coupled optical emission spectroscopy (ICP-OES) and their composition is reported in Table 1.

The synthesis method of the $ErPO_4$ crystals is important, as previous studies show that potential excess P in microcrystalline REE phosphate powders leads to apparent non-stochiometric dissolution trends in previous experiments (Poitrasson et al., 2004; Cetiner et al., 2005). This issue is mitigated by employing the synthesis method by Cherniak et al. (2004), as is evidenced by several studies using synthetic mm-sized $REEPO_4$ crystals (Gysi et al., 2015, 2018; Van Hoozen et al., 2020; Gysi and Harlov, 2021; Banerjee et al., 2025). The pure and euhedral mm-sized crystals of $ErPO_4$ were synthesized at the GFZ Helmholtz Centre for Georesearch, Potsdam, Germany using the same method as previously described in Cherniak et al. (2004). $ErPO_4$ (possibly hydrated) was precipitated from a warm 1:1 molar mixture of a $Er(NO_3)_3$ solution and $NH_4H_2PO_4$ solution, which was subsequently dried to a very fine grained powder. The dried $ErPO_4$ powder was then ground up and approximately 0.9 grams mixed with 25 grams of a Pb-free 75/25 Na_2CO_3/MoO_3 flux. The mix was then placed in a Pt crucible and heated to 1375 °C in open air over a 4 h period. The crucible remained at this temperature for 15 h and was then cooled to 870

°C over one week at 3 °C/h, which allowed crystals of $ErPO_4$ to nucleate and grow. The flux containing the $ErPO_4$ crystals was boiled in water until they were freed from the flux. The crystals were subsequently analyzed using an electron microprobe analyzer for purity in Gysi et al., (2015), indicating that there were no trace elements in the $ErPO_4$ up to the detection limit of less than 0.08 wt.%. In this study the $ErPO_4$ crystals were analyzed using Raman spectroscopy and scanning electron microscopy equipped with an energy-dispersive X-ray spectrometer.

2.2. Experimental method

Hydrothermal solubility experiments were conducted in Inconel-625 Parr Instruments batch-type reactors and follow similar procedures as previous studies (Gysi et al., 2015, 2018; Van Hoozen et al., 2020; Gysi and Harlov, 2021). The interior volume (~77.23 ±0.01 cm^3) was determined by adding deionized water to each autoclave and recording the mass. Sample holders for the $ErPO_4$ crystals were made from annealed titanium foil (Alfa Aesar 99.7% purity) with a length of ~10 cm, and a pocket at the top, which has been punctured with a needle to facilitate equilibration. The pocket is designed to sit above the experimental solution at ambient temperature and becomes submerged at experimental conditions due to the expansion of the fluid allowing for interaction of the fluid with the $ErPO_4$ crystal (Fig. 1). Prior to loading, the sample holders are oxidized in air at 300 °C to create a TiO_2 coating, which reduces interaction of the holder with solutions. The holders were then placed into the batch-type reactors, which were filled with 30 to 45 ml of solution depending on temperature, pressure, and salinity conditions for each experimental run (Fig. 1).

The solution amounts at 350 °C were set to 35 ml as experiments were conducted at P_{sat} and this solution volume was sufficient to raise the solution gas interface above the sample holder

in the experiments. At 400 and 450 °C, the solution volume was calculated using the SoWat software package (Driesner, 2007; Driesner and Heinrich, 2007) for NaCl-H_2O fluids to be equivalent to 500 bar. The internal volume of the autoclaves was determined, as described above, and masses of Ti sample holders (0.16–0.27 g) and $ErPO_4$ crystals (0.05–0.15 g) were accounted for during pressure calculations. Fluid densities are 576 kg/m^3 at 350 °C, 579 kg/m^3 at 400 °C and 404–473 kg/m^3 at 450 °C, which are higher than the critical density of water (322 kg/m^3). Therefore, the HKF model is suitable for thermodynamic calculations (Helgeson et al., 1981; Miron et al., 2019). Experimental run conditions and results are summarized in Table 4 and fluid density, salinity, and mole fraction of NaCl (X_{NaCl}) reported in Supplementary Material Table S14.

The head assembly of each autoclave was coated with nickel anti-seize lubricant (Loctite LB N-5000) and the head space was purged using N_2 gas (Airgas research grade) for 2 min prior to sealing the reactors. The reactors were placed in a high temperature muffle furnace (Thermo Scientific Lindberg/Blue M). Temperature was recorded using an Omega temperature logger with K-type thermocouples ensuring constant temperature within 2 °C at experimental conditions. The duration of experiments was more than 7 days based on kinetic experiments for low temperature experiments in Gysi et al. (2015) who used the same solids and similar sample holder designs, indicating steady state conditions were reached after 10 days at 100 °C and 5 days at 160 °C.

After quenching in a cold-water bath with ice, the autoclaves were opened, the sample holder was removed, and the experimental solutions were extracted and weighed. The pH of the experimental solutions was measured, and the solutions were acidified to 2% nitric acid (HNO_3 Fisher Chemical 65–70% trace metal grade). An aliquot of the experimental fluid (~10–15 ml) was filtered (ThermoFisher Target2 Cellulose Acetate Syringe Filters 0.2 µm) for analysis using inductively coupled plasma-mass spectrometry (ICP-MS) to measure the Er concentration. The

autoclaves were subsequently treated using a H_2SO_4-washing technique to extract all $ErPO_4$ that precipitated onto the walls during quenching. Precipitation of REE solids during quenching in Cl-bearing experiments is well documented in other experimental studies (Migdisov et al., 2009; Banerjee et al., 2025). The use of H_2SO_4-bearing solutions is commonly employed to extract all REE before starting a new experiment. The development of the H_2SO_4-washing technique used in this study is described in more detail in the Supplementary Material (Figure S1, Table S1). For extraction of precipitated $ErPO_4$, the autoclaves were filled with 66 ml of 1% sulfuric acid (H_2SO_4; J.T. Baker 93–98% trace metals grade) solution, sealed and placed into the furnace at 160 °C for four days. After quenching, these 'hot wash' solutions were extracted and filtered for analysis. This procedure was repeated a second time. Finally, 4 ml of concentrated sulfuric acid was used to wash the interior of each autoclave after the second hot wash. The concentrated sulfuric acid solutions were diluted to a concentration of ~1% H_2SO_4 and filtered for analysis. Of the total Er, ~5% is extracted with the experimental solution, ~71% is extracted in the first 'hot wash', ~22% in the second 'hot wash' and less than 3% in the last concentrated sulfuric acid wash (Supplementary Material Table S1).

Experimental duplicates are within ~2% for all experiments with a salinity of 0.01 mol/kg and 0.1 mol/kg NaCl and within <5% for 0.5 mol/kg NaCl. Between experimental runs, autoclaves were soaked for 24 h in ~1% H_2SO_4 solutions, rinsed, and soaked in Milli-Q before being rinsed again and dried before the next experiment. Autoclave head assemblies were cleaned in an ultrasonic bath (Branson Ultrasonics™ CPX952318R) to remove the lubricant. Autoclaves were passivated in air at ≥300 °C to form a Ni-Cr oxide layer before each experiment increasing the chemical resistance of the interior autoclave walls (Liu et al., 2024; Kim et al., 2024). Titanium sample holders were soaked in ~3% HNO_3 ACS grade solution for a minimum of 3 h, and

subsequently soaked in MilliQ and dried before reuse. $ErPO_4$ crystals were rinsed with MilliQ, dried and weighed before being reused or analyzed using Raman Spectroscopy and SEM/EDS.

2.3. Analytical methods

The pH of experimental starting solutions was measured at ambient temperature using a Mettler Toledo pH meter and Mettler Toledo electrode with an integrated temperature sensor (precision of ±0.01). The electrode was calibrated using commercial buffer solutions from Fisher Scientific (pH of 4.01 ±0.01, 7.00 ±0.01, and 10.01 ±0.02). The pH of the experimental starting solutions with pH 2, 3, and 4 was measured before NaCl was added. The pH of the most alkaline solutions was prepared on the day of the experiment by titration of a NaOH-solution to the saline solutions to adjust pH to the desired measured values. The measured pH (25 °C) for each experimental solution is listed in Table 1. The pH (T) is calculated at experimental temperature and pressure using the GEM-Selektor code package based on measured values of pH (25 °C), see below for thermodynamic calculations.

Sodium concentrations of the starting solutions were measured using an Agilent 5900 ICP-OES at the New Mexico Bureau of Geology and Mineral Resources. The concentration range for Na standards measured was from 1.25 to 50 ppm with uncertainties ranging from 0.5–2 %. The NaCl bearing experimental solutions were diluted such that Na concentrations were within the calibration standard curve. Salinities were calculated from the measured Na concentrations and are listed in Table 1.

Quenched experimental and wash solutions were measured using an Agilent 7900 ICP-MS at the New Mexico Bureau of Geology and Mineral Resources. Calibrations for ICP-MS analyses

were carried out using a multi element REE standard and an in-line internal standard Ir-In solution. Two Er isotopes (166, 167) were measured using the standard mode and the He gas collision cell, which reduces interferences from REE-oxides forming in the plasma. Due to the low concentrations of Er in each solution, no observed interferences or impacts of oxide formation, ^{166}Er in standard mode was used. Drift correction was performed using the ^{193}Ir isotope and blank corrections were performed based on repeatedly measuring 2% HNO_3 blanks. The limit of detection (LOD) is based on 3σ of the blank solutions at 0.1 ppt Er and the limit of quantification (LOQ) is based on 9σ of the blank solutions at 0.4 ppt Er. The analytical uncertainty of experimental solutions (0.0002 to 0.161 ppb) ranged from 0.1% to 8.9% with an average of 3.4%. Hot washes (washes 1 and 2), which had the highest Er concentrations (0.004 to 2.236 ppb) had uncertainties ranging from 0.05% to 4.7% with an average of 1.7%. The cold wash which used concentrated sulfuric acid (wash 3), which had the lowest Er concentrations (0 to 0.193 ppb) had uncertainties ranging from 0.5% to 26% with an average of 7.6%. Data reduction was conducted using the Agilent MassHunter software package. Phosphorous was analyzed in experimental solutions but was below the LOD of 4.2 ppb P, due to various N-O and O interferences with blank intensities of 12,000 to 15,000 cps similarly observed in previous studies (Gysi et al., 2018). Total Er concentrations in the experimental solutions at temperature and pressure were calculated by adding measured Er concentrations from the quenching experimental solutions, the two 1% sulfuric acid 'hot wash' solutions, and the concentrated sulfuric acid wash solutions.

Solids were analyzed using Raman spectroscopy to ensure that the $ErPO_4$ crystals are pure before and after experiments and to show that no other Er minerals formed. Raman analysis was conducted using a Horiba LabRAM HR Evolution confocal Raman spectrometer equipped with a 532 nm green laser, an 1800 grooves/mm grading and an Olympus LMPlanFL 50x long working

distance objective (NA =0.5; WD = 10.6 mm). The unreacted crystals were characterized between 50–4500 cm^{-1} and reacted crystals were analyzed between 820 and 1400 cm^{-1} focused on the symmetric and asymmetric stretching vibrational modes of xenotime. Laser intensity was set to 10–25% with an acquisition time of 5 s and three acquisitions. The instrument was calibrated using a Horiba SP-RCO NIST traceable polystyrene 1921b with a band position at 1001.4 ±0.5 cm^{-1} and the 520.5 cm^{-1} band of a silica wafer. Analytical uncertainty is 0.35 cm^{-1} for the given frequency of 820 and 1400 cm^{-1} based on repeated measurement of the Si standard.

Scanning Electron Microscope-Energy Dispersive Spectrometry (SEM-EDS) was performed with a JEOL JSM-IT700HR Field Emission SEM at 15 kV accelerating voltage, 10.0–10.7 mm working distance, and high vacuum to ensure the purity of $ErPO_4$ solids (Pt coated) and to evaluate if secondary solids precipitated on the surface of the crystals after quenching (Fig. 3). Semi-quantitative compositional data was collected by SEM-EDS on identified solids and $ErPO_4$ crystals using an Oxford X-MaxN silicon drift detector for and calculated using Aztec 6.1 software.

2.4. Thermodynamic calculations

Aqueous speciation, activities, pH at temperature and pressure, and $ErPO_4$ solubility were calculated using the GEM-Selektor v.3 code package (Kulik et al., 2013). The thermodynamic properties of aqueous species and solids considered for pH and speciation calculations of experimental solutions and for GEMSFITS optimization are summarized in Table 2. Additional species and solids used in the simulations of natural ore-fluids and applications to REE deposits were taken from the MINES thermodynamic database (Gysi et al., 2023;

https://geoinfo.nmt.edu/mines-tdb). Thermodynamic properties of aqueous Er species were compiled from different sources and evaluated against experimental data comprising the MINES database, which is compared to the SUPCRT92 database slop98 (Johnson et al., 1992; Sverjensky et al., 1997) including thermodynamic properties of Er complexes from Haas et al. (1995). The MINES compilation (Gysi et al., 2023) considers updated thermodynamic properties for Er^{+3} from Pan et al. (2024), for $ErCl^{+2}$ and $ErCl_2^{+}$ from Migdisov et al. (2009) and Migdisov and Williams-Jones (2006), and the compilation of Haas et al. (1995) for the hydroxyl complexes. The ErO_2^{-} (i.e., $Er(OH)_4^{-}$) and $ErCl_3^{0}$ species were not considered in the speciation calculations based on slope relationships of experiments (Section 3.3). Thermodynamic properties for $ErPO_{4(s)}$ include heat capacity, enthalpy, entropy, and volume from 0–1600 K (Ni et al., 1995; Ushakov et al., 2001; Gavrichev et al., 2012).

The thermodynamic properties for aqueous species were calculated at the temperature and pressure of interest using the revised HKF model (Helgeson et al., 1981; Shock and Helgeson, 1988; Tanger and Helgeson, 1988; Shock et al., 1992). The properties of H_2O were calculated using the IAPS-84 equation-of-state (Kestin et al., 1984). A detailed evaluation of thermodynamic and electrostatic models on high temperature activity calculations is discussed in Miron et al. (2019) indicating that the model assumptions herein are adequate for the temperature and pressure range of the experiments. In the GEM-Selektor code package, the TSolMod library was used to retrieve equations of state and activity models (Wagner et al., 2012). The activity coefficients of aqueous species (γ_i) were calculated in GEM-Selektor using the extended Debye-Hückel equation (Robinson and Stokes, 1968),

$$log\gamma_i = \frac{Az_i^2\sqrt{I}}{1+\mathring{a}B\sqrt{I}} + \Gamma_\gamma + b_\gamma I \quad (1)$$

where A and B are the Debye-Hückel parameters (Helgeson and Kirkham, 1974; Helgeson et al., 1981); b_γ is the temperature-pressure dependent extended term parameter dependent on the background electrolyte; å is the ion size parameter; Γ_γ is a conversion factor for mole fraction to molality (Helgeson et al., 1981; Wagner et al., 2012). The ion size parameter, å, was selected to be consistent with the NaCl background electrolyte (3.72), parameter b_γ and activity coefficients γ_i for species were automatically calculated by a subroutine and activity coefficients for water was calculated from the osmotic coefficient in GEM-Selektor (Helgeson et al., 1981). All experimental solutions contain NaCl (0.01–0.5 mol/kg), which is why the NaCl background electrolyte was selected from available background electrolyte models including KCl, NaOH, and KOH. The NaCl background electrolyte model and associated thermodynamic properties of Na and Cl species were updated and tested up to 800 °C and 5 kbar in Miron et al. (2016). The ionic strengths *I* is calculated in GEM-Selektor using

$$I = \frac{1}{2}\sum_i m_i z_i^2 \quad (2)$$

where m_i is the molality in mol/kg H_2O and z_i is the charge of the i^{th} aqueous species.

2.5. Speciation reactions and species formation constants

The following deprotonation reactions of orthophosphoric acid control phosphate speciation in experimental solutions:

$$H_3PO_4^0 \rightleftharpoons H^+ + H_2PO_4^- \quad (3)$$

$$H_2PO_4 \rightleftharpoons H^+ + HPO_4^{-2} \quad (4)$$

At experimental conditions, Eq. (3) is most relevant with the neutral $H_3PO_4^0$ species stable at lower pH (<5) and $H_2PO_4^-$ stable at higher pH (>7). The dominant phosphoric acid species at each T-P condition assessed were calculated for the range of pH values using GEM-Selektor. The equilibrium pH for Eq. (3) increases from 5.5 to 5.8 and finally to 7.2 at 350, 400 and 450 °C, respectively. The dominant phosphate species subsequently impacts the reaction stoichiometry for $ErPO_4$ dissolution reactions.

The dissolution reactions of $ErPO_4$ depend on the dominant Er and phosphate species present at experimental conditions and are summarized below:

$$ErPO_{4(s)} \rightleftharpoons Er^{+3} + PO_4^{-3} (K_{s0}) \quad (5)$$

$$ErPO_{4(s)} + 3H^+ \rightleftharpoons Er^{+3} + H_3PO_4^0 \quad (6)$$

$$ErPO_4 + xCl^- + 3H^+ \rightleftharpoons ErCl_x^{(3-x)} + H_3PO_4^0 \quad (7)$$

$$ErPO_{4(s)} + yH_2O_l + (3-y)H^+ \rightleftharpoons Er(OH)_y^{(3-y)} + H_3PO_4^0 \quad (8)$$

$$ErPO_{4(s)} + yH_2O_l + (3-y)H^+ \rightleftharpoons Er(OH)_y^{(3-y)} + H_2PO_4^- + H^+ \quad (9)$$

The solubility product (K_{s0}) is defined by Eq. (5). However, in the experimental solutions $ErPO_4$ solubility is controlled by different Er and phosphate species (Eqs. 6–9). Based on previous works (Wood, 1990; Haas, 1995; Gammons et al., 2002; Migdisov et al., 2009, 2016; Han and Gysi, 2024, 2025) the stochiometric coefficient (x) in Er chloride dominated dissolution reactions can vary between 1 and 3 (Eq. 7) and the coefficient (y) in Er hydroxyl dominated reactions varies between 1 and 4 (Eqs. 8–9). The speciation of Er is dependent on pH and chloride activity with Er^{+3} and Er chloride species predominant at moderately acidic conditions (pH of 2–5) and Er hydroxyl species at near-neutral to alkaline conditions (pH >5). In the pH region where $H_3PO_4^0$

predominates, $ErPO_4$ dissolution is governed by Eqs. (6–7) corresponding with a stochiometric relationship of 3 pH for Er^{+3} and Er chloride species. $ErPO_4$ solubility governed by Eq. (8) shows a stoichiometric relationship of 2 pH for $Er(OH)^{+2}$, 1 pH for $Er(OH)_2^{+}$, is pH-independent for the neutral $Er(OH)_3^0$ species, and -1 pH for $Er(OH)_4^-$. In pH region where $H_2PO_4^-$ predominates, the stoichiometric relationship with pH changes to -1 pH for the neutral species $Er(OH)_3^0$ and to -2 pH for the $Er(OH)_4^-$ species (Eq. 9). Fitted slopes in $ErPO_4$ solubility-pH diagrams are used to derive the average stoichiometry of dissolution reactions for Er hydroxyl species, and the average stoichiometry of Er chloride species is determined from pH corrected log m_{Er} as a function of logarithmic chloride activity (Section 3.3).

Species formation constants (β_n) according to Eqs. (7) for chloride and (8–9) for hydroxyl are calculated using optimized standard Gibbs energies derived using GEMSFITS (Miron et al., 2015) as described in Section 2.6, based on the experimental solubility data at 350, 400, and 450 °C using the following equation:

$$log\beta_i^{Cl,OH} = \frac{-\Delta G_r^0}{RTln(10)} \quad (10)$$

The logarithm of the Er chloride and hydroxyl species formation constants ($log\beta_n^{Cl,OH}$) are fitted as a function of temperature using the following equation:

$$log\beta_i^{Cl,OH} = A_0 + A_1 \cdot t + A_2 \cdot t^{-1} \quad (11)$$

where A_0, A_1, and A_2 are the fitted coefficients and t is the temperature in Kelvin (K).

2.6 Thermodynamic optimization

The GEMSFITS code package (Miron et al., 2015, https://gems.web.psi.ch/GEMSFITS/) uses the GEMS3K chemical solver implemented in GEM-Selektor (Kulik et al., 2013) and is a program for parameter optimization of thermodynamic properties. The GEMSFITS program uses the bound optimization by quadratic approximation (Powell, 2009) to solve for optimizations with the sum of residuals as the target parameter to minimize in each iterative loop until convergence is reached. GEMSFITS outputs parameter correlation coefficients and a composite scaled sensitivity factor (CSS), which are key statistic parameters to evaluate the sensitivity and covariance of optimized species (Tiedeman and Hill, 2007; Miron et al., 2015).

The standard Gibbs energy of formation ($\Delta_f G^0_{T,P}$) was optimized at experimental conditions for the following Er chloride and Er hydroxyl species: $ErCl^{+2}$, $ErCl_2^{+}$, $Er(OH)^{+2}$, $Er(OH)_2^{+}$, and $Er(OH)_3^{0}$. The optimization procedure follows a similar approach as described in previous studies (Miron et al., 2015; Gysi et al., 2018; Pan et al., 2024). At each experimental temperature and pressure, the input concentrations of Er, NaCl, HCl, and NaOH are used to calculate the equilibrium solubility of $ErPO_4$. The calculated total dissolved Er concentrations are then compared with the measured experimental Er concentrations and the $\Delta_f G^0_{T,P}$ values are then adjusted for the selected Er chloride and hydroxyl species. After this step, equilibrium is re-calculated until a best fit is reached by minimizing differences between measured and calculated Er concentrations. The conditions for the optimization calculations are summarized in Table 3.

At 350 °C, the Er chloride species displayed very low CSS values. Nevertheless, optimizing the thermodynamic properties for these species results in residuals for Er concentrations that are considerably improved. Therefore, the $\Delta_f G^0_{T,P}$ values for Er chloride species were optimized first using a 5 kJ/mol upper/lower bounds within the value determined experimentally in the study by Migdisov et al. (2009) while keeping the thermodynamic properties

of Er hydroxyl species constant at initial literature values. A second optimization task was created using the previously fitted $\Delta_f G^0_{T,P}$ values for Er chloride species, while the $\Delta_f G^0_{T,P}$ values for Er hydroxyl species were optimized to best fit the solubility data at near-neutral to alkaline pH. In this step, $Er(OH)^{+2}$ was constrained within 5 kJ of database values (due to its low sensitivity) while both $Er(OH)_2^+$ and $Er(OH)_3^0$ species could be freely fitted to the experimental data. For solubility data retrieved at 400 and 450 °C and 0.01 mol/kg NaCl, Er chloride species were optimized first and Er hydroxyl species were optimized in a second task. No upper/lower boundary constraints were needed due to the higher CSS values for at least one Er chloride and hydroxyl species in these fits.

3. RESULTS

3.1. $ErPO_4$ crystals and dissolution textures

Raman analysis was conducted on unreacted and reacted crystals to ensure purity and structural characteristics of the crystal remain consistent before and after experiments (Fig. 2). The unreacted $ErPO_4$ crystals show two main peaks at 1002 and 1059 cm^{-1} for symmetric (v_1-PO_4) and asymmetric (v_3-PO_4) stretching vibrations of the PO_4 tetrahedron. These peak center positions for both Raman modes are within 0.3 cm^{-1} of the unreacted crystal (Fig. 2b, Table S2) and consistent with those reported in Hurtig et al. (2024). Characteristic fluorescence for $ErPO_4$ occurs between 400 and 800 cm^{-1} and 3400 and 3800 cm^{-1} (Fig. 2a). The reacted crystals for the intermediate pH ranges show lower peak intensities compared to the unreacted crystals, which has been observed in crystals reacted at high temperature in previous studies (Strzelecki et al., 2022). Importantly, no additional peaks were observed that would indicate additional Er or P phases (Er oxides,

hydroxides, and churchite) and the peak center positions are within the analytical uncertainty of ~0.35 cm^{-1} before and after reaction (Table S2).

Secondary electron (SEM) imaging of unreacted and reacted $ErPO_4$ crystals exhibit a tetragonal crystal habit consistent with the xenotime structure (Fig. 3a-b). The crystal surfaces of the unreacted crystals are clean and display growth steps but no dissolution pits or edging is visible (Fig. 3c), which is consistent with previous observations of crystals synthesized using the same method (Gysi et al., 2015). Reacted crystals retain their tetragonal crystal habit and dissolution textures are only visible along the edges of crystals at macroscopic scales (Fig. 3b) and at microscopic scales on crystal surfaces (Fig. 3d-f). At alkaline pH, the surface shows less than 0.50 µm dissolution pits on some surfaces and dissolution etching along crystal growth steps (Fig. 3d). At near-neutral to mildly acidic conditions, no dissolution textures are observed. At mildly acidic conditions, dissolution pitting on all crystal surfaces show rounded to elongated pits of less than 0.50 µm in size (Fig. 3e). At acidic conditions, dissolution pits occur pervasively across the entire crystal surface (Fig. 3f) and connect along cleavage planes and edges. Dissolution pits are prismatic and reach up to ~2 µm in length (Fig. 3f). Variations in dissolution pit size, form, and habit coincide with pH differences in the starting solutions, providing evidence of pH dependent dissolution as observed in the Er concentrations from solution analyses. Dissolution textures indicate that solutions with starting pH of 2 with the strongest features reflect the highest $ErPO_4$ solubility, whereas pH 3 and pH 4 solutions show decreasing evidence of dissolution textures indicating less substantial dissolution of $ErPO_4$. These observations are consistent with other mineral solubility studies conducted in hydrothermal acidic to alkaline solutions (Gysi et al., 2015; Payne et al., 2023).

Careful SEM-EDS and Raman spectroscopic characterization of the mm-sized synthetic $ErPO_4$ crystals after experiments show no indication of secondary REE or P phases or REE/P enriched or depleted patches on the surface of the reacted crystals. These observations indicate that the formation of leached layers or buffering of the solution by new secondary minerals were not an issue and therefore non-stochiometric dissolution is unlikely to be significant or present.

3.2. $ErPO_4$ solubility experiments

Two sets of experiments were conducted to evaluate the effect of pH, temperature, and salinity on Er solubility between 350 and 450 °C. The first set was conducted at constant salinity of 0.01 mol/kg NaCl and varying starting pH of 2, 3, 4 and 10 at 350 °C and water vapor saturation pressure (P_{sat}), and at 400 and 450 °C at 500 bar. The second set of experiments was conducted at 450 °C and 500 bar varying salinity between 0.01, 0.1 and 0.5 mol/kg and varying starting pH of 2, 3, 4 and 10. Results are presented in Table 4 and Figure 4. $ErPO_4$ solubility ranges between 0.03 and 5.3 ppb Er and increases with temperature and salinity. Duplicate experiments were conducted at 400 °C and 0.01 mol/kg NaCl, 450 °C and 0.01, 0.1, and 0.5 mol/kg NaCl and a starting pH of 2. Propagated analytical precision reported in Table 4 ranges between 0.2 and 3.1 % and the experimental reproducibility based on duplicate experiments is 3% for all experiments except in solutions with 0.5 mol/kg NaCl where duplicates yield a 5% uncertainty.

Experiments with the most acidic solutions (pH 2.45–4.48; starting pH 2) show the highest Er concentrations (1.1–5.3 ppb) in all experiments (Fig. 4). The calculated pH increases with temperature for solutions with starting pH values of 2, 3, and 4 and decreases for experiments with a starting pH value of ~10 (Table 4). This results in an overall studied pH range from ~2.5 to 8 at

temperatures between 350 and 450 °C and becomes narrower in solutions with 0.01 to 1 mol/kg NaCl with calculated pH values ranging between ~4 to 8 at 450 °C (Fig. 4). Experiments conducted at constant salinity of 0.01 mol/kg show a decrease in $ErPO_4$ solubility with increasing pH at 350 °C from 2.2 to 0.1 ppb Er. At 400 and 450 °C, Er concentrations initially decrease as pH values approach ~6 and then increase again at more alkaline conditions (pH >7.5), showing a solubility minimum at near-neutral pH (Fig. 4a). At 450 °C, the $ErPO_4$ solubility minimum at near-neutral pH conditions is more pronounced compared to the lower temperature experiments (Fig. 4).

Experiments conducted at 450 °C with variable salinity show pH shifting to higher values with increasing chloride content. The $ErPO_4$ solubility minimum is shifted to higher pH values with increasing chloride concentration (Fig. 4b). $ErPO_4$ solubility also increases with increasing Cl^- content at 450 °C and reaches the highest concentrations in solutions with 0.5 mol/kg (5.3 ppb aqueous Er) NaCl at acidic pH and is lowest (0.03 ppb Er) in solutions with 0.01 mol/kg NaCl at near-neutral pH. At a constant starting pH of 2, 3, and 4, Er concentrations increase ~1 order of magnitude when comparing between 0.01 and 0.5 mol/kg NaCl solutions (Fig. 4b). However, at more alkaline starting pH 10 the 0.01 mol/kg NaCl solution shows the highest Er concentrations (Fig. 4b), which indicates that Er chloride species are important at acidic to mildly acidic pH (2–4) and Er hydroxyl species are controlling the increased Er concentrations at alkaline pH (>7.5).

3.3 Derivation of Er speciation stoichiometry

The dissolution of $ErPO_4$ is controlled by Eqs. (5–9) depending on the major aqueous Er and phosphate species as a function of pH and chloride concentration. The average stoichiometry of aqueous Er species was derived based on a linear regression of log m_{Er} vs. pH for Er hydroxyl

487 species and based on a linear regression of a pH-corrected log m_{Er} vs. loga_{Cl^-} for Er^{+3} and Er
488 chloride species (Fig. 5; Table 5). The species formation constants (β_n) cannot directly be extracted
489 from the slope relationships due to the presence of multiple species controlling solubility, and the
490 fact that solubilities were plotted in the mixed activity-concentration coordinates, leading to
491 deviations from stoichiometric slopes. Rather, these relationships are used to guide GEMSFITS
492 optimization.

493 Across the entire pH range between 1 and 3 discrete slopes are observed (Fig. 5a-d; Table
494 5). At 350 and 400 °C in 0.01 mol/kg NaCl solutions, the solubility data can be fitted to a slope of
495 approximately -0.95 to -1.03 at acidic pH (2–4 at 25 °C), and a pH independent slope close to ~0
496 at more alkaline conditions with pH of 4–8 (Fig. 5a, b). These slope relationships indicate that
497 $ErPO_4$ solubility is controlled by $ErOH_2^+$ and $ErOH_3^0$ species (Eqs. 8–9). At 450 °C in the 0.01
498 mol/kg NaCl solutions, the solubility data correspond to a slope of -1.49 at mildly acidic pH (4–
499 5), a pH independent slope of 0 at near-neutral pH (5–6), and a slope of +0.84 at more alkaline pH
500 (6–8) (Fig. 5c). These slope relationships are controlled by the contribution of several different Er
501 hydroxyl and/or chloride species at acidic conditions (i.e., $ErCl^{+2}$, $ErCl_2^+$, $ErOH^{+2}$ and $ErOH_2^+$;
502 (Eqs. 7–8) and $ErOH_3^0$ at near-neutral pH, respectively (Eq. 9). The positive slope at alkaline pH
503 can be attributed to a change in phosphate species from $H_3PO_4^0$ to $H_2PO_4^{-1}$ (Eq. 3). No evidence
504 of the $Er(OH)_4^-$ species was found based on these slope relationships. As indicated by Eq. (9), a
505 positive slope of 2 would be expected in Figure 5c at alkaline conditions in the $H_2PO_4^{-1}$
506 predominance field.

507 At 450 °C, the slope at mildly acidic conditions (pH 4–5) decreases from -1.49 in 0.01
508 mol/kg NaCl solutions to -1.06 in the 0.1 mol/kg NaCl solutions and finally to -0.54 in the 0.5
509 mol/kg NaCl solutions (Table 5). A significant increase in Er concentrations with increasing

chloride concentration suggests an increased stability of $ErCl^{+2}$ and $ErCl_2^+$ species at higher concentrations of Cl^-. However, chloride content also impacts the calculated pH at elevated temperature and pressure shifting $ErPO_4$ solubility curves towards higher pH and moving Er speciation from chloride to hydroxyl species. Similar observations were made by Banerjee et al. (2025) for $NdPO_4$ solubility in NaCl-bearing solutions at 500 to 700 °C.

The stoichiometry of Er chloride species was derived from the fitted slopes in a pH-corrected log $m_{Er,}$-log a_{Cl^-} diagram at the lowest pH of 3.9–4.5 (Fig. 5d). The average slope of -1.12 from the log m_{Er}-pH diagrams at 450 °C and different chloride concentrations was used to correct log m_{Er} for extracting the dependency on the chloride activity. Linear regression of pH-corrected log m_{Er} with chloride activity shows a slope of 1.52 indicating an average stoichiometric coefficient x of 1–2 related to Eq. (7) and the presence of $ErCl_2^+$ and $ErCl^{+2}$. If $ErCl_3^0$ would be present, a stoichiometric coefficient of 2–3 would be expected.

The slope relationships indicate contributions of primarily the Er hydroxyl species $ErOH_2^+$ and $ErOH_3^0$ at 350 to 450 °C and moderately acidic to alkaline pH 3–8. At more acidic conditions (pH 2–3), the presence of $ErCl^{+2}$ and $ErCl_2^+$ are indicated by the increase in slopes at lower pH and the increase of $ErPO_4$ solubility with increasing chloride concentration. Importantly, no evidence was found for $ErCl_3^0$ and $Er(OH)_4^-$ (i.e., ErO_2^-) species. This information was subsequently used in the GEMSFITS optimization discussed in Section 4.2.

4. DISCUSSION

4.1 Comparison of predicted and experimental $ErPO_4$ solubility

$ErPO_4$ solubility was predicted at experimental conditions using different thermodynamic databases, including the SUPCRT92 database and the MINES thermodynamic database with references provided in Table 2. Importantly, the $ErCl_3^0{}_{(aq)}$ and ErO_2^- (i.e., $Er(OH)_4^-$) species are included in the SUPCRT92 database, but are excluded in the MINES database, because there was no evidence for their presence in the slope relationships (Fig. 5).

At each experimental temperature and pressure, the predicted $ErPO_4$ solubility (log m_{Er}) is compared to experimentally measured Er concentrations using the difference $\Delta_{\text{predicted-experimental}}$ (Fig. 6). At 350 °C and low pH (~2), predicted Er concentrations are ~1 log unit higher than experimentally measured Er concentrations for both the SUPCRT92 and the MINES database indicating similar predicted stabilities for $ErCl_2^+$ and $ErCl^{+2}$ (Supplementary Material Tables S10–11). With an increase in temperature, the predicted log m_{Er} values remain within ~0.7 log units at 400 °C. Finally, the models underpredict log m_{Er} by up to one order of magnitude at 450 °C (Fig. 6b-c). At 350 and 400 °C, both databases predict $ErCl_2^+$ and $ErCl^{+2}$ to control speciation, however, at 450 °C, SUPCRT92 predicts $ErCl_3^0$ to be dominant. Thermodynamic properties of $ErCl_3^0$ were last updated in Haas et al. (1995). However, UV-vis spectroscopy indicates the presence of $ErCl_2^+$ and $ErCl^{+2}$ at 150–250 °C, whereas $ErCl_3^0$ was not found to be detectable at those temperatures (Migdisov and Williams-Jones, 2006). Guan et al. (2022) used molecular dynamic simulations and EXAFS to investigate La speciation in Cl-bearing solutions and found that at 350–450 °C, and an NaCl concentration of 0.01 mol/kg, both $LaCl^{+2}$ and $LaCl_2^+$ predominate, whereas $LaCl_3^0$ becomes stable at greater than 500 °C in more saline solutions. The slope relationships at 450 °C in this study indicate an average stochiometric factor of x = 1.5 for $ErCl_x^{(3-x)}$ complexes (Fig. 5d), supporting the decision to remove the $ErCl_3^0$ species from predictive calculations at the experimental conditions.

554 At alkaline conditions (pH >7), the predicted Er concentrations are 2.5 log units higher
555 than the experimentally measured $ErPO_4$ solubility using the SUPCRT92 database, and ~1 log unit
556 higher than the predicted Er concentrations using the MINES database. This discrepancy is related
557 to the presence of the ErO_2^- (i.e., $Er(OH)_4^-$) species in the SUPCRT92 database, which is not
558 considered in MINES. Slope relationships described in this study indicate that $Er(OH)_4^-$ is not
559 present at experimental conditions and that the slightly positive slope of 0.84 at 450 °C is more
560 likely related to the change in dominant phosphate species as described in Eq. (9) (Fig. 5c). Han
561 and Gysi (2024, 2025) also showed that the $Er(OH)_4^-$ is not present at an alkaline pH of up to 9–
562 9.5 at 25–75 °C using UV-vis spectroscopy. At 400 and 450 °C and alkaline pH (>7), the difference
563 between predicted and measured $ErPO_4$ solubility decreases with increasing temperature from 1.5
564 to 0.8 log units for the SUPCRT92 database and from 0.4 to -0.2 log units for the MINES database
565 (Fig. 6b,c).

566 The number and type of Er^{+3} species was updated in Pan et al. (2024) using a similar
567 GEMSFITS optimization procedure to this study based on $ErPO_4$ solubility data from Gysi et al.
568 (2015). Here we show a comparison of the predicted log m_{Er} using the MINES database, which
569 includes the Pan et al. (2024) update for Er^{+3}, plotted against the SUPCRT92 database and against
570 the experimental data using perchlorate solutions (Gysi et al., 2015). The MINES database closely
571 matches the experimental data, whereas the SUPCRT92 database shows discrepancies of 8 log
572 units in comparison to the experimental data. In Cl-bearing solutions at elevated temperature, the
573 Er chloride species are predicted to be more stable than the Er^{+3} species, which is also shown by
574 the slope relationships in our experiments, indicating that Er hydroxyl and chloride species are
575 stable (Fig. 5).

576

4.2 Optimization of $\Delta_f G^0_{T,P}$ of Er chloride and hydroxyl species

The starting point for the GEMSFITS optimization of the thermodynamic properties for Er chloride and hydroxyl species was the MINES thermodynamic database utilizing the Er species listed in Table 2. The optimization procedure focuses on addressing discrepancies between predicted log $m_{Er,}$ using the MINES database, and the experimentally measured $ErPO_4$ solubility as a function of temperature, pH, and salinity (Fig. 6). The slope relationships, and evaluation of the existing thermodynamic data, led to the decision to remove $ErCl_3^0$ and $Er(OH)_4^-$ species from the optimization procedure. The standard Gibbs energies of formation for $ErCl^{+2}$, $ErCl_2^+$, $Er(OH)^{+2}$, $Er(OH)_2^+$, and $Er(OH)_3^0$ were optimized at temperature and pressure ($\Delta_f G^0_{T,P}$) and are summarized in Table 6. In addition to the updated $\Delta_f G^0_{T,P}$, the original Gibbs energy as calculated using the MINES database, the difference $\Delta_{opt\text{-}MINES}$ in Gibbs energy, and the CSS factor is listed in Table 6.

At 350 °C, optimizations for $ErCl^{2+}$ and $ErCl_2^+$ display low CSS values, indicating low sensitivities for the given experimental data. The calculated corrections for the $\Delta_f G^0_{T,P}$ values reach values of 5 kJ mol^{-1} more positive than the extrapolated values using the HKF parameters derived from the experimental study of Migdisov et al. (2009). These adjustments are within the experimental uncertainty of Migdisov et al. (2009). The optimized $\Delta_f G^0_{T,P}$ values for Er hydroxyl species, $Er(OH)^{2+}$ and $Er(OH)_2^+$ (i.e., ErO^+), are more negative by -3.3 and -19.0 kJ mol^{-1}, respectively, in comparison to the values calculated from the MINES database based on Haas et al., (1995). The optimized $\Delta_f G^0_{T,P}$ values for $Er(OH)_3^0$ (i.e., ErO_2H^0) are significantly more positive by 44.6 kJ mol^{-1} in comparison to the values calculated from Haas et al. (1995). The Er hydroxyl species with the highest sensitivity at 350 °C is $Er(OH)_2^+$ whereas the CSS values for other Er hydroxyl species are quite low indicating significant uncertainties in the optimized values.

At 400 °C, the $ErCl^{+2}$ species has the highest sensitivity with optimized $\Delta_f G^0_{T,P}$ values needing an adjustment of -17.9 kJ mol^{-1}, whereas the $ErCl_2^+$ species displays a low sensitivity and a small adjustment of <1 kJ mol^{-1} in comparison to predicted $\Delta_f G^0_{T,P}$ values calculated from the MINES database. The optimized $\Delta_f G^0_{T,P}$ values for Er hydroxyl species display similar adjustments to the optimizations at 350 °C; albeit the $Er(OH)_3^0$ (i.e., ErO_2H^0) species displays a smaller correction of 11.0 kJ mol^{-1} and higher sensitivity (Table 6). The CSS values are highest for $ErCl^{+2}$ and $Er(OH)_2^+$ followed by ErO_2H^0, indicating that the optimization was more sensitive towards these species, which is consistent with slope relationships derived from the experimental data.

At 450 °C, the optimized $\Delta_f G^0_{T,P}$ values for $ErCl^{+2}$ remains within 1 kJ mol^{-1} of the value calculated from the MINES database, whereas $ErCl_2^+$ shows a significant adjustment of -37.1 kJ mol^{-1} and a high CSS values, implying a higher stability of the latter species. The optimization of Er hydroxyl species are similar to those at 400 °C with the exception of $Er(OH)_2^+$ (i.e., ErO^+), which is 5 kJ mol^{-1} more positive than the $\Delta_f G^0_{T,P}$ value calculated from the MINES database. The optimized $\Delta_f G^0_{T,P}$ values for Er chloride species indicate an increased stability of $ErCl_2^+$ at 450 °C, which is in line with the slope relationships derived from fits to the experimental solubility data (Fig. 5 and Table 5; slope of ~2).

The optimized Gibbs energies of formation were implemented into GEM-Selektor to predict $ErPO_4$ solubility at experimental conditions and compared to the experimental data (Fig. 6). The deviation of predicted and measured log m_{Er} is generally within experimental uncertainty indicating an improvement compared to previous thermodynamic databases (Fig. 7). However, at 350 °C and low pH (<3), the predicted log m_{Er} still overestimates the measured $ErPO_4$ solubility because the correction of $\Delta_f G^0_{T,P}$ for Er chloride species was restricted to 5.0 kJ mol^{-1}. At 450 °C

and an alkaline pH (>7), the optimized model shows a slight increase in solubility at these conditions, however, it is insufficient to reach the experimentally measured log m_{Er}. Therefore, it is possible that the $Er(OH)_4^-$ (i.e., ErO_2^-) species is indeed stable at these conditions. Experimental data presented in this study were not sufficiently detailed to adequately optimize this species.

4.3. Derivation of high temperature formation constants (log$\beta^{Cl,OH}$) for Er chloride and hydroxyl complexes

The optimized $\Delta_f G^0_{T,P}$ values from Table 6 are used to calculate the cumulative formation constants (log$\beta^{Cl,OH}$) of Er chloride and hydroxyl species according to Eq. (10) (Table 7) and fitted according to Eq. (11) as a function of temperature with coefficients given in Table 8. The species formation constants are compared to literature values of between 25 and 450 °C in Figure 8.

The first formation constant for the $ErOH^{+2}$ species (β_1^{OH}), calculated using a combination of Er^{+3} from Pan et al. (2024), and $Er(OH)_2^+$ derived from (Haas et al., 1995), generally follows a trend between 100 and 300 °C that approaches our experimental values at higher temperature (Fig. 8a). In contrast, using the Er^{+3} aqua ion from SUPCRT92 (slop98.dat; Johnson et al. 1992), results in much higher β_1^{OH} values. The second and third Er hydroxyl formation constants (β_2^{OH} and β_3^{OH}), calculated between 100 and 300 °C, significantly diverge from the trends derived based on the optimization of our experimental solubility data at higher temperature (Fig. 8c, e). At supercritical conditions, the β_1^{OH}–β_3^{OH} values, derived from our study, were not fitted together with the lower temperature extrapolations, which are based on the HKF parameters by Haas et al. (1995). Instead we provide temperature dependent log β_1^{OH}–β_3^{OH} functions for interpolation between 350 and 450 °C.

The formation constants for Er chloride species (β_1^{Cl} and β_2^{Cl}), calculated based on the HKF parameters derived in Migdisov et al. (2009), show a significant divergence with our experimental data at 350 °C (Fig. 8b,d). We display these fits only between 100 and 350 °C because their HKF parameters were derived from low temperature experimental data at saturated water vapor pressure (Gammons et al., 2002; Migdisov and Williams-Jones, 2006; Migdisov et al., 2009). Comparison of these extrapolations at 350 °C with our experimental data indicates up to two orders of magnitude difference with the values derived in this study. The $\log\beta_1^{Cl}$ and $\log\beta_2^{Cl}$ functions fitted between 350 and 450 °C, based on our experimental study, indicate that the stability of the $ErCl_2^+$ species exponentially increases in supercritical fluids, which was not captured previously. Due to low sensitivity of the Er chloride species at 350 °C during GEMSFITS optimization, there is additional uncertainty in the $\log\beta_1^{Cl}$ and $\log\beta_2^{Cl}$ at this temperature, whereas the formation constants are much better constrained at 400 and 450 °C.

A possible reason that the high temperature data cannot be fitted together with the lower temperature data is due to pressure effects in the supercritical region, and the need for further experiments as a function of pressure. In conclusion, we do not recommend the use of our solubility fits beyond the fitted region of 350–450 °C or at pressures outside of what is explored in this study (P_{sat} at 350 °C; 500 bar at 400 and 450 °C). $ErPO_4$ solubility predicted using the optimized formation constants fitted in this study (Table 7) generally result in predictions that stay within 1 log unit at 350 °C, 0.3 log units at 400 °C, and 0.5 log units at 450 °C of the experimentally measured Er concentrations (Fig. 6b-d; red points).

4.4. Er speciation in experimental solutions

667 The updated thermodynamic data for Er aqueous species listed in Tables 7–8 were implemented
668 into the GEM-Selektor code package for predicting Er solubility and speciation in experiments
669 and testing optimized thermodynamic data (Fig. 7). Modeled Er speciation based on SUPCRT92
670 (slop98.dat; Johnson et al., 1992), the MINES thermodynamic database, and the optimized
671 thermodynamic data from this study are compared at 350, 400, and 450 °C and 0.01 mol/kg NaCl
672 in Figure 9.

673 At acidic to weakly acidic conditions (pH <4) and 350 °C, Er chloride species predominate
674 based on SUPCRT92, Er chloride and Er^{+3} aqua ion predominate based on MINES, and Er^{+3}
675 predominates with subordinate Er chloride species based on the optimized data from this study
676 (Fig. 9a-c). At 400 °C, speciation is dominated in all models by Er chloride species, however
677 $ErCl^{+2}$ dominates in SUPCRT92 and this study, whereas $ErCl_2^{+}$ dominates in the simulations using
678 MINES (Fig. 9d-f). At 450 °C, the $ErCl_3^0$ species dominates based on SUPCRT92, whereas the
679 $ErCl^{+2}$ species dominates in the MINES and optimized simulations (Fig. 9g-i).

680 The shift from Er chloride to hydroxyl species occurs around a pH of ~4 based on
681 SUPCRT92 and MINES at all temperatures, whereas it is shifted to a lower pH value of 3 at 350
682 °C and a higher pH value of ~5 at 450 °C when using the optimized data derived from this study
683 (Fig. 9). At neutral pH (~3–6) and 350 and 400 °C, the $Er(OH)_3^0$ species predominates with
684 subordinate $Er(OH)_2^{+}$, based on SUPCRT92 and MINES, whereas the stability field of the
685 $Er(OH)_2^{+}$ species is significantly expanded in the optimized speciation calculations (Fig. 9c). At
686 450 °C, the stability field of $Er(OH)_2^{+}$ decreases in all simulations and the $Er(OH)_3^0$ species is
687 predominant.

688 At alkaline conditions (pH >6), $Er(OH)_4^{-}$ becomes increasingly predominant over $Er(OH)_3^0$
689 in the simulations using SUPCRT92 at increasing pH from ~5.5 to 6.5 between 350 and 450 °C.

690 The $Er(OH)_3^0$ species predominates at all temperatures in the simulations using MINES. The
691 optimized speciation calculations show a switchover in predominance from $Er(OH)_2^+$ to $Er(OH)_3^0$
692 at a pH of ~9 at 350 °C, a pH of ~6.8 at 400 °C and at 450 °C; the $Er(OH)_3^0$ species predominates
693 at all neutral to alkaline conditions (Fig. 9i).

694

695 **4.5. Implications for modeling the solubility of REE in ore-forming fluids**

696 Geochemical simulations at subcritical and supercritical conditions were conducted using the
697 GEM-Selektor code package. At subcritical conditions, thermodynamic properties for Er species
698 were taken from the MINES database (Table 2) and at supercritical conditions updated
699 thermodynamic properties from this study were used (Table 7–8). Two rock titration simulations
700 were performed at i) 250 °C and P_{sat} and ii) at 450 °C and 700 bar using an NaCl-bearing fluid
701 with a salinity of 5 wt% NaCl (0.85 mol/kg) and a pH of 1 at 25 °C (0.1 mol/kg HCl). A simplified
702 pegmatite with a composition comparable to a pegmatite from the Strange Lake deposit in Canada
703 (Gysi and Williams-Jones, 2013) with $ErPO_4$ added was titrated from 0–600 g into 1 kg of acidic
704 saline fluid (Fig. 10).

705 At 250 °C, the rock titration model buffers pH from 1.3 to 3.3 after addition of ~85 g of
706 pegmatite to 1 kg of acidic saline fluid, i.e. with a fluid to rock ratio (F/R) of ~34. At this high F/R
707 (>12; <85 g of rock added), the mineralogy is comprised of quartz, hematite, and fluorite (Fig.
708 10a). At intermediate F/R (12–5; 85–200 g of rock added), pH increases slowly from 3.3 to 4.7
709 and the mineralogy is comprised of quartz, hematite, $ErPO_4$, fluorite, and muscovite-paragonite.
710 At low F/R (<3; ;>200 g rock added), pH is constant at ~4.8 and the mineralogy is comparable to
711 unaltered pegmatite i.e., quartz, hematite, muscovite, albite, microcline, and $ErPO_4$. Aqueous Er

speciation at 250 °C is dominated by $ErCl_2^+$ (60 % of speciation) and $ErCl^{+2}$ (22 % of speciation) at low pH and high F/R greater than 3 (Fig. 10c). At low F/R (<3) and a pH of 4.7, $Er(OH)_3^0$ (57 % of speciation) and $Er(OH)_2^+$ (23 % of speciation) control solubility. The $ErPO_4$ solubility ranges from -5.2 to -9.5 log m_{Er} and is highest at a low pH <3 and a high F/R greater than 12, and sharply decreases with decreasing F/R and increasing pH.

At 450 °C and high F/R (>22, 45 g rock added), the mineralogy is comprised of quartz, hematite, and $ErPO_4$ (Fig. 10b). At intermediate F/R (22–1.8; 45–555 g of rock added), the mineralogy is comprised of quartz, hematite, $ErPO_4$, fluorite, muscovite, and albite. At high F/R (F/R <1.8; >550 g of rock added), the mineralogy is consistent with unaltered pegmatite. The pH at 450 °C is higher at all F/R compared to the 250 °C model, due to decreased acid dissociation constants. At low F/R, pH increases rapidly from 3.8 to 5.4, then marginally increases to 5.7 with decreasing F/R from 22 to 1.7 (Fig. 10f). The species $ErCl_2^+$ dominates at low pH (<5 and high F/R >22) and at intermediate F/R. $ErCl_2^+$ and $Er(OH)_3^0$ species coexist with similar abundances of 50–60 mol%. At low F/R, the $Er(OH)_3^0$ species controls Er mobility (Fig. 10d). The $ErPO_4$ solubility decreases from -7.2 log m_{Er} at high F/R and low pH to -9.6 log m_{Er} at low F/R and neutral pH (>5).

$ErPO_4$ solubility is primarily controlled by pH neutralization as a result of fluid-rock equilibration at sub- and supercritical conditions. The solubility of $ErPO_4$ decreases by four orders of magnitude at 250 °C and by 2.5 orders of magnitude at 450 °C due to pH neutralization (>4). The pH effect is more pronounced at subcritical conditions due to increased acid dissociation constants, therefore requiring more rock to neutralize the pH. These simulations are consistent with observations from the Strange Lake REE deposit, where HREE were mainly mobilized at lower temperatures in highly acidic fluids due to the retrograde dissolution of zircon and the release

of HREE remobilized into the surrounding granite (Gysi and Williams-Jones, 2013; Gysi et al., 2016; Vasyukova and Williams-Jones, 2018). The rock-buffered pH of 4.8 and 5.1 at 250 and 450 °C, respectively, cannot easily be overstepped as it is dependent on the rock buffering mineralogy and pegmatite composition. However, a hydrothermal fluid, which interacts with peralkaline and alkaline rocks consisting of microcline, arfvedsonite, and aegirine, may result in more alkaline pH values as observed in thermodynamic models based on fluid inclusion data from the Strange Lake deposit (Vasyukova and Williams-Jones, 2018). The capacity for rock to buffer fluid pH therefore limits the mobility of Er under alkaline conditions.

5. Conclusions

This study provides new measurements of the solubility of the $ErPO_4$ in Cl-bearing solutions of varying starting pH (2, 3, 4 and 10) and salinity (0.01, 0.1, and 0.5 mol/kg NaCl) at temperatures from 350 to 450 °C. The solubility of $ErPO_4$ is controlled by the aqueous species which predominate at a given pH and salinity. The Er-chlorides ($ErCl^{+2}$, $ErCl_2^{+}$) control solubility, which decreases with increasing pH between 2 and 4. At neutral to alkaline conditions (pH 6–8), $ErPO_4$ solubility levels off at 350 and 400 °C or increases again at 450 °C as hydroxyl species become stable ($Er(OH)^{+2}$, $Er(OH)_2^{+}$, $Er(OH)_3^{0}$). The chloride content also exerts and important control on Er concentrations, which increase 5-fold as a function of increasing salinity from 0.01 to 0.5 mol/kg NaCl at 450 °C. These results indicate increased stability of Er chloride complexes at acidic conditions.

Extrapolations of HKF parameters to pressure and temperature conditions beyond the P-T range of underlying experimental data result in large discrepancies between experimental data and

computational predictions. This demonstrates that these parameters cannot always be extrapolated beyond the P-T range in which they were derived. To resolve these discrepancies, the thermodynamic properties of Er chloride and hydroxyl species were optimized in this study. The optimized thermodynamic properties expand the applicability for thermodynamic predictions to 450 °C and 500 bar, where Er solubility and speciation in supercritical hydrothermal fluids can be more accurately predicted. The fitted formation constant functions derived here emphasize the increased importance of $Er(OH)_2^+$ and $Er(OH)_3^0$ in mildly acidic to near neutral fluids at 350 and 400 °C, whereas $ErCl_2^+$ displays greater stability at the expense of Er-hydroxyl species at 450 °C. This study provides important new insights into HREE mobility in hydrothermal supercritical fluids and the controls on HREE mobility as a function of temperature, salinity, and pH, and is broadly applicable to natural settings through optimized thermodynamic functions provided herein.

Acknowledgements

This research is based upon work supported by the U.S. Department of Energy, Office of Science, Office of Basic Energy Sciences, Geosciences program under Award Number DE-SC0022269 to AG and NH. We also acknowledge NSF/EAR-MRI 2117061 to NH and AG, which supported the purchase of the Raman spectrometer. We thank B. Frey, D. Bacca and H. Han for help with ICP-MS and ICP-OES analyses and method development, M. Woodard and N. Iverson for help with SEM analyses and S. Smith-Schmitz for help with Raman Spectroscopy analyses and data evaluation at the New Mexico Bureau of Geology. We thank two anonymous reviewers for their comments and associate editor Dr. Klein for handling our manuscript.

Author contributions

CK performed experiments and analyses of this study, contributed to conceptualization, methodology and writing of the manuscript. NH and AG conceptualized this study, and contributed to experiments, analyses, methodology and writing of the manuscript. AM and LW contributed to writing of the manuscript. DH made the $ErPO_4$ crystals used in the experiments and contributed to the writing of the manuscript. AG, NH, AM and LW acquired funding for this project.

Conflicts of Interest

There are no competing interests to declare.

Appendix A. Supplementary Material

The Supplementary Materials section of this paper includes information on washing techniques used to remove re-precipitated Er during quenching and information on Raman spectra collected on $ErPO_4$ solids. The data availability provides an excel version of all main tables and supplemental tables.

The Supplementary Materials document contains:

i) Detailed description of washing techniques developed in this study and corresponding Figure S1 and Table S1

ii) Detailed description of Raman spectra collected on $ErPO_4$ solids and corresponding Table S2.

DATA AVAILABILITY

Electronic tables and additional background data are found in the data availability. This includes:

i) Tables 1–8 from the Manuscript.

ii) Tables S1–S2 from the Supplementary Materials document.

iii) Tables S3–S8 which are the experimental and literature data used in Figures 4–6.

iv) Tables S9–S13 which show the optimized Er species data and other thermodynamic predictions used to plot Figures 6–10.

v) Table S14 which summarizes solution density and compositions used in pressure calculations.

Data are available through Mendeley Data using doi: https://doi.org/10.17632/r6r429f223.1

References

Andersen, A.K., Clark, J.G., Larson, P.B., Neill, O.K., 2016. Mineral chemistry and petrogenesis of a HFSE(+HREE) occurrence, peripheral to carbonatites of the Bear Lodge alkaline complex, Wyoming. Am. Min. 101, 1604–1623.

Banerjee, Y., Ghosh, P., Krishnan, S., Viladkar, S.G., 2025. $NdPO_4$ solubility and aqueous neodymium speciation in supercritical fluids: An experimental study at 500–700 °C and 1.7 kbar. Geochim. Cosmochim. Acta 350, 145–163.

Bera, M.K., Luo, G., Schlossman, M.L., Soderholm, L., Lee, S., Antonio, M.R., 2015. Erbium(III) Coordination at the Surface of an Aqueous Electrolyte. J. Phys. Chem. B 119, 8734–8745.

Cherniak, D.J., Pyle, J., Rakovan, J., 2004. Synthesis of REE and Y phosphates by Pb-free flux methods and their utilization as standards for electron microprobe analysis and in design of monazite chemical U-Th-Pb dating protocol. Am. Min. 89, 1533–1539.

Cetiner, Z.S., Wood, S.A., Gammons, C.H., 2005. The aqueous geochemistry of the rare earth elements. Part XIV. The solubility of rare earth element phosphates from 23 to 150 °C. Geochim. Cosmochim. Acta 69, 345–358.

Di, J. and Ding, X., 2024. Complexation of REE in hydrothermal fluids and its significance on REE mineralization. Minerals, 14(6), 531.

Driesner, T. and Heinrich, C.A., 2007. The system H_2O–NaCl. Part I: Correlation formulae for phase relations in temperature–pressure–composition space from 0 to 1000 °C, 0 to 5000 bar, and 0 to 1 XNaCl. Geochim. et Cosmochim. Acta 71, 4880-4901.

Driesner, T., 2007. The system H_2O–NaCl. Part II: Correlations for molar volume, enthalpy, and isobaric heat capacity from 0 to 1000 °C, 1 to 5000 bar, and 0 to 1 XNaCl. Geochim. et Cosmochim. Acta *71*, 4902-4919.

Gammons, C.H., Wood, S.A. and Li, Y., 2002. Complexation of the rare earth elements with aqueous chloride at 200 °C and 300 °C and saturated water vapor pressure. In: Hellmann, R. and Wood, S.A. (Eds.), Water–Rock Interaction, Ore Deposits, and Environmental Geochemistry: A Tribute to David A. Crerar. Geochemical Society Special Publication No. 7, Geochemical Society, Houston, 191–207.

839 Gavrichev, K.S., Ryumin, M.A., Tyurin, A.V., Gurevich, V.M., Khoroshilov, A.V., Komissarova,
840 L.N., 2012. Thermodynamic functions of erbium orthophosphate $ErPO_4$ in the temperature
841 range of 0–1600K. Thermochim. Acta 535, 1–7.
842 Guan, Y., Mei, Y., Duan, Z., Pan, D., 2022. Speciation and thermodynamic properties of La(III)–
843 Cl complexes in hydrothermal fluids: A combined molecular dynamics and in-situ X-ray
844 absorption spectroscopy study. Geochim. Cosmochim. Acta 337, 1–16.
845 Gysi, A.P., Hurtig, N.C., Pan, R., Miron, G.D., Kulik, D.A., 2023, MINES thermodynamic
846 database, New Mexico Bureau of Geology and Mineral Resources, version 23,
847 https://doi.org/10.58799/mines-tdb.
848 Gysi, A.P., Harlov, D., 2021. Hydrothermal solubility of $TbPO_4$, $HoPO_4$, $TmPO_4$, and $LuPO_4$
849 xenotime endmembers at pH of 2 and temperatures between 100 and 250 °C. Chem. Geol.
850 567, 120072.
851 Gysi, A.P., Harlov, D., Miron, G.D., 2018. The solubility of monazite ($CePO_4$), $SmPO_4$, and
852 $GdPO_4$ in aqueous solutions from 100 to 250 °C. Geochim. Cosmochim. Acta 242, 143–
853 164.
854 Gysi, A.P., Williams-Jones, A.E., 2013. Hydrothermal mobilization of pegmatite-hosted REE and
855 Zr at Strange Lake, Canada: A reaction path model. Geochim. Cosmochim. Acta 122, 324–
856 352.
857 Gysi, A.P., Williams-Jones, A.E., Collins, P., 2016. Lithogeochemical Vectors for Hydrothermal
858 Processes in the Strange Lake Peralkaline Granitic REE-Zr-Nb Deposit. Econ. Geol. 111,
859 1241–1276.

Gysi, A.P., Williams-Jones, A.E., Harlov, D., 2015. The solubility of xenotime-(Y) and other HREE phosphates ($DyPO_4$, $ErPO_4$ and $YbPO_4$) in aqueous solutions from 100 to 250 °C and p_{sat}. Chem. Geol. 401, 83–95.

Haas, J.R., Shock, E.L., Sassani, D.C., 1995. Rare earth elements in hydrothermal systems: Estimates of standard partial molal thermodynamic properties of aqueous complexes of the rare earth elements at high pressures and temperatures. Geochim. Cosmochim. Acta 59, 4329–4350.

Halter, W.E., Williams-Jones, A.E., Kontak, D.J., 1998. Origin and evolution of the greisenizing fluid at the East Kemptville tin deposit, Nova Scotia, Canada. Econ. Geol. 93, 1026–1051.

Han, H.J., Gysi, A.P., 2024. UV-Vis spectrophotometric determination of rare earth elements (REE) speciation at near-neutral to alkaline pH. Part I: m-cresol purple properties from 25–75 °C and Er hydrolysis. Dalton Trans. 53, 13129–13141.

Han, H.J., and Gysi, A.P., 2025. UV-Vis spectrophotometric determination of rare earth elements (REE) speciation at near-neutral to alkaline pH. Part II: hydrolysis of Er from 25 to 75° C. Dalton Trans. 54, 5153-5163.

Haque, N., Hughes, A., Lim, S., Vernon, C., 2014. Rare Earth Elements: Overview of Mining, Mineralogy, Uses, Sustainability and Environmental Impact. Resour. 3, 614–635.

Harlov, D.E, Meighan, C.J., Kerr, I.D., Samson, I.M., 2016. Mineralogy, chemistry, and fluid-aided evolution of the Pea Ridge Fe oxide-(Y + REE) deposit, Southeast Missouri, USA. Econ. Geol. 111, 1963–1984.

Helgeson, H.C., Kirkham, D.H., 1974. Prediction of the thermodynamic properties of electrolytes at high pressures and temperatures. Phys. Chem. Earth 13–14, 133–177.

Helgeson, H.C., Kirkham, D.H., Flowers, G.C., 1981. Theoretical prediction of the thermodynamic behavior of aqueous electrolytes by high pressures and temperatures; IV, Calculation of activity coefficients, osmotic coefficients, and apparent molal and standard and relative partial molal properties to 600 °C and 5kb. Am. J. Sci. 281, 1249–1516.

Hofstra, A.H., Meighan, C.J., Song, X., Samson, I., Marsh, E.E., Lowers, H.A., Emsbo, P. and Hunt, A.G., 2016. Mineral thermometry and fluid inclusion studies of the Pea Ridge iron oxide-apatite–rare earth element deposit, Mesoproterozoic St. Francois Mountains terrane, Southeast Missouri, USA. Econ. Geol., 111(8), pp.1985–2016.

Hurtig, N.C., Gysi, A.P., Smith-Schmitz, S.E., Harlov, D., 2024. Raman spectroscopic study of anhydrous and hydrous REE phosphates, oxides, and hydroxides. Dalton Trans. 53, 9964–9978.

Johnson, J.W., Oelkers, E.H., Helgeson, H.C., 1992. SUPCRT92: A software package for calculating the standard molal thermodynamic properties of minerals, gases, aqueous species, and reactions from 1 to 5000 bar and 0 to 1000 °C. Comput. Geosci. 18, 899–947.

Jowitt, S.M., 2022. Mineral economics of the rare-earth elements. MRS Bull. 47, 276–282.

Kestin, J., Sengers, J.V., Kamgar-Parsi, B., Sengers, J.M.H.L., 1984. Thermophysical Properties of Fluid H_2O. JPCRD 13, 175–183.

Kim, S., Park, J., Lee, S., 2024. Examination of oxide formation in oxidation of Inconel 600 and 625 at high temperatures using phase diagrams. Coatings 14, 621.

Kulik, D.A., Wagner, T., Dmytrieva, S.V., Kosakowski, G., Hingerl, F.F., Chudnenko, K.V., Berner, U.R., 2013. GEM-Selektor geochemical modeling package: revised algorithm and GEMS3K numerical kernel for coupled simulation codes. Comput. Geosci. 17, 1–24.

Lee, J.H., Byrne, R.H., 1992. Examination of comparative rare earth element complexation behavior using linear free-energy relationships. Geochim. Cosmochim. Acta 56, 1127–1137.

Liu, W., Zhang, H., Li, Q., 2024. Comparative study on microstructure and oxidation resistance of Inconel 625 superalloy coatings on 12CrMoV steel surfaces prepared by CMT and MIG cladding. Surf. Coat. Technol. 492, 129757.

Migdisov, A., Williams-Jones, A., Wagner, T., 2009. An experimental study of the solubility and speciation of the Rare Earth Elements (III) in fluoride- and chloride-bearing aqueous solutions at temperatures up to 300 °C. Geochim. Cosmochim. Acta 73, 7087–7109.

Migdisov, A., Williams-Jones, A.E., Brugger, J., Caporuscio, F.A., 2016. Hydrothermal transport, deposition, and fractionation of the REE: Experimental data and thermodynamic calculations. Chem. Geol. 439, 13–42.

Migdisov, A.A., Williams-Jones, A.E., 2006. A spectrophotometric study of erbium (III) speciation in chloride solutions at elevated temperatures. Chem. Geol. 234, 17–27.

Miron, G.D., Kulik, D.A., Dmytrieva, S.V., Wagner, T., 2015. GEMSFITS: Code package for optimization of geochemical model parameters and inverse modeling. Appl. Geochem. 55, 28–45.

Miron, G.D., Wagner, T., Guillaume, D., 2016. Internally consistent thermodynamic data for aqueous species in the system Na–K–Al–Si–O–H–Cl. Geochim. Cosmochim. Acta 187, 258–273.

Miron, G.D., Allan M.L., Alina Y., 2019. Thermodynamic properties of aqueous species calculated using the HKF model: how do different thermodynamic and electrostatic models for solvent water affect calculated aqueous properties? Geofluids, 5750390.

927 Moore, M., Chakhmouradian, A.R., Mariano, A.N. and Sidhu, R., 2015. Evolution of rare-earth
928 mineralization in the Bear Lodge carbonatite, Wyoming: Mineralogical and isotopic
929 evidence. Ore Geol. Rev., 64, 499–521.
930 Ni, Y., Hughes, J.M., Mariano, A.N., 1995. Crystal chemistry of the monazite and xenotime
931 structures. American Mineralogist 80, 21–26.
932 Pan, R., Gysi, A.P., Miron, G.D., Zhu, C., 2024. Optimized thermodynamic properties of REE
933 aqueous species (REE^{+3} and $REEOH^{2+}$) and experimental database for modeling the
934 solubility of REE phosphate minerals (monazite, xenotime, and rhabdophane) from 25 to
935 300 °C. Chem. Geol. 643, 121817.
936 Payne, M.R., Gysi, A.P., Hurtig, N.C., 2023. Hydrothermal fluorite solubility experiments and
937 mobility of REE in acidic to alkaline solutions from 100 to 250 °C. Chem. Geol. 617,
938 121256.
939 Perry, E.P., Gysi, A.P., 2018. Rare Earth Elements in Mineral Deposits: Speciation in
940 Hydrothermal Fluids and Partitioning in Calcite. Geofluids, 5382480.
941 Poitrasson, F., Oelkers, E.H., Schott, J., Montel, J.M., 2004. Experimental determination of
942 synthetic $NdPO_4$ monazite end-member solubility in water from 21 to 300 °C: Implications
943 for rare earth element mobility in crustal fluids. Geochim. Cosmochim. Acta 68, 2207–
944 2221.
945 Powell, M.J.D., 2009. The BOBYQA algorithm for bound constrained optimization without
946 derivatives. Cambridge England, Technical Report NA2009/06, 26–46.
947 Robie, R.A., Hemingway, B.S., 1995. Thermodynamic properties of minerals and related
948 substances at 298.15 K and 1 bar (10^5 Pa) pressure and at higher temperatures. Vol. 2131.
949 US Government Printing Office, Washington, DC.

Robinson, R.A., Stokes, R.H., 1968. Electrolyte Solutions: Second Rev. Ed. Dover Publications Inc., New York.

Rudolph, W., Irmer, G., 2019. On the Hydration of Heavy Rare Earth Ions: Ho^{+3}, Er^{+3}, Tm^{+3}, Yb^{+3} and Lu^{+3} - A Raman Study. Molecules 24, 1953.

Shock, E.L., Helgeson, H.C., 1988. Calculation of the thermodynamic and transport properties of aqueous species at high pressures and temperatures: Correlation algorithms for ionic species and equation of state predictions to 5 kb and 1000 °C. Geochim. Cosmochim. Acta 52, 2009–2036.

Shock, E.L., Oelkers, E.H., Johnson, J.W., Sverjensky, D.A., Helgeson, H.C., 1992. Calculation of the thermodynamic properties of aqueous species at high pressures and temperatures. Effective electrostatic radii, dissociation constants and standard partial molal properties to 1000 °C and 5 kbar. J. Chem. Soc., Faraday Trans. 88, 803–826.

Smith, M.P., Henderson, P., Peishan, Z., 1999. Reaction relationships in the Bayan Obo Fe-REE-Nb deposit Inner Mongolia, China: Implications for the relative stability of rare-earth element phosphates and fluorocarbonates. Contrib. Mineral. Petrol. 134, 294–310.

Smith, R.M., Martell, A.E., 1976. The Selection of Critical Stability Constants. In: Chemical Equilibrium and Reaction Models. John Wiley & Sons, Ltd, New Jersey, 7–29.

Soderholm, L., Skanthakumar, S., Wilson, R.E., 2009. Structures and Energetics of Erbium Chloride Complexes in Aqueous Solution. J. Phys. Chem. A 113, 6391–6397.

Strzelecki, A.C., Reece, M., Zhao, X., Yu, W., Benmore, C., Ren, Y., Alcorn, C., Migdisov, A., Xu, H., Guo, X., 2022. Crystal Chemistry and Thermodynamics of HREE (Er, Yb) Mixing in a Xenotime Solid Solution. ACS Earth Space Chem. 6, 1375–1389.

Sverjensky, D.A., Shock, E.L., Helgeson, H.C., 1997. Prediction of the thermodynamic properties of aqueous metal complexes to 1000 °C and 5 kb. Geochim. Cosmochim. Acta 61, 1359–1412.

Tagirov, B.R., Zotov, A.V., Akinfiev, N.N., 1997. Experimental study of dissociation of HCl from 350 to 500 °C and from 500 to 2500 bars: thermodynamic properties of HCl(aq). Geochim. Cosmochim. Acta 61, 4267–4280.

Tanger, J.C., Helgeson, H.C., 1988. Calculation of the thermodynamic and transport properties of aqueous species at high pressures and temperatures; revised equations of state for the standard partial molal properties of ions and electrolytes. Am. J. Sci. 288, 19–98.

Tiedeman, C.R. and Hill, M.C., 2007. Model calibration and issues related to validation, sensitivity analysis, post-audit, uncertainty evaluation and assessment of prediction data needs. In: S.M. Gorelick (Ed.), Groundwater: Resource Evaluation, Augmentation, Contamination, Restoration, Modeling and Management. International Association of Hydrological Sciences Publication 312, Wallingford, UK, pp. 237–282.

Ushakov, S.V., Helean, K.B., Navrotsky, A., Boatner, L.A., 2001. Thermochemistry of rare-earth orthophosphates. JMR 16, 2623–2633.

Van Hoozen, C.J., Gysi, A.P., Harlov, D.E., 2020. The solubility of monazite ($LaPO_4$, $PrPO_4$, $NdPO_4$, and $EuPO_4$) endmembers in aqueous solutions from 100 to 250 °C. Geochim. Cosmochim. Acta 280, 302–316.

Vasyukova, O.V., Williams-Jones, A.E., 2018. Direct measurement of metal concentrations in fluid inclusions, a tale of hydrothermal alteration and REE ore formation from Strange Lake, Canada. Chem. Geol. 483, 385–396.

Wagner, T., Kulik, D.A., Hingerl, F.F., Dmytrieva, S.V., 2012. GEM-Selektor geochemical modeling package: TSolMod library and data interface for multicomponent phase models. Can. Mineral. 50, 1173-1195.

Williams-Jones, A., Migdisov, A., Samson, I., 2012. Hydrothermal Mobilisation of the Rare Earth Elements - a Tale of "Ceria" and "Yttria". Elem. 8, 355–360.

Wood, S.A., 1990. The aqueous geochemistry of the rare-earth elements and yttrium: 1. Review of available low-temperature data for inorganic complexes and the inorganic REE speciation of natural waters. Chem. Geol. 82, 159–186.

FIGURES

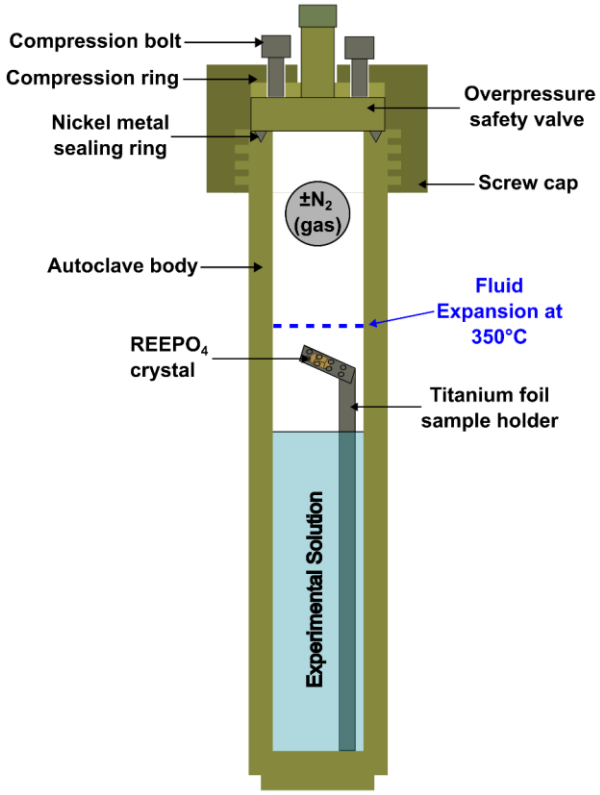

Figure 1. Diagram of the experimental setup used for Er solubility experiments using batch-type Inconel-625 reactors. Experiments were degassed with N_2 gas to remove atmospheric oxygen. The solid $ErPO_4$ crystal was contained in a Ti foil sample holder. Fluid expansion at 350 °C is illustrated by the blue dashed line. Due to the 400 °C and 450 °C experiments being above the supercritical fluid point, solutions expanded into the entire autoclave.

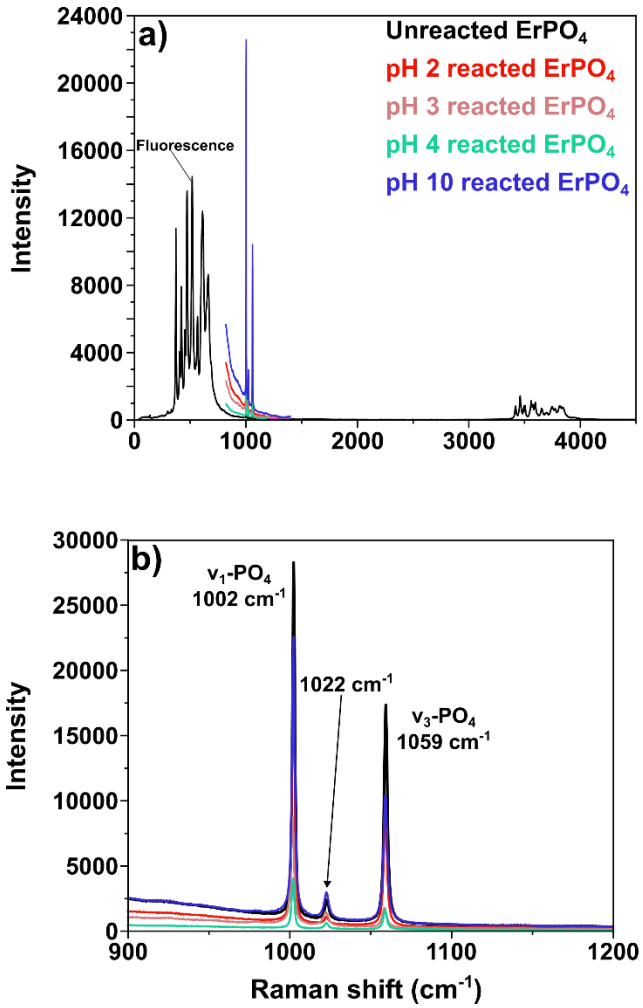

1029

1030 Figure 2. Raman spectroscopy peaks comparing unreacted and reacted $ErPO_4$ crystals showing: a)
1031 the full spectrum with fluorescence and b) a segment of the spectrum which highlights
1032 characteristic PO_4 peaks. Peak center positions of the ν_1-PO_4 vibrational band are at 1002 ± 0.35
1033 cm^{-1} and 1059 ± 0.35 cm^{-1} for the ν_3-PO_4 vibrational band.

1034

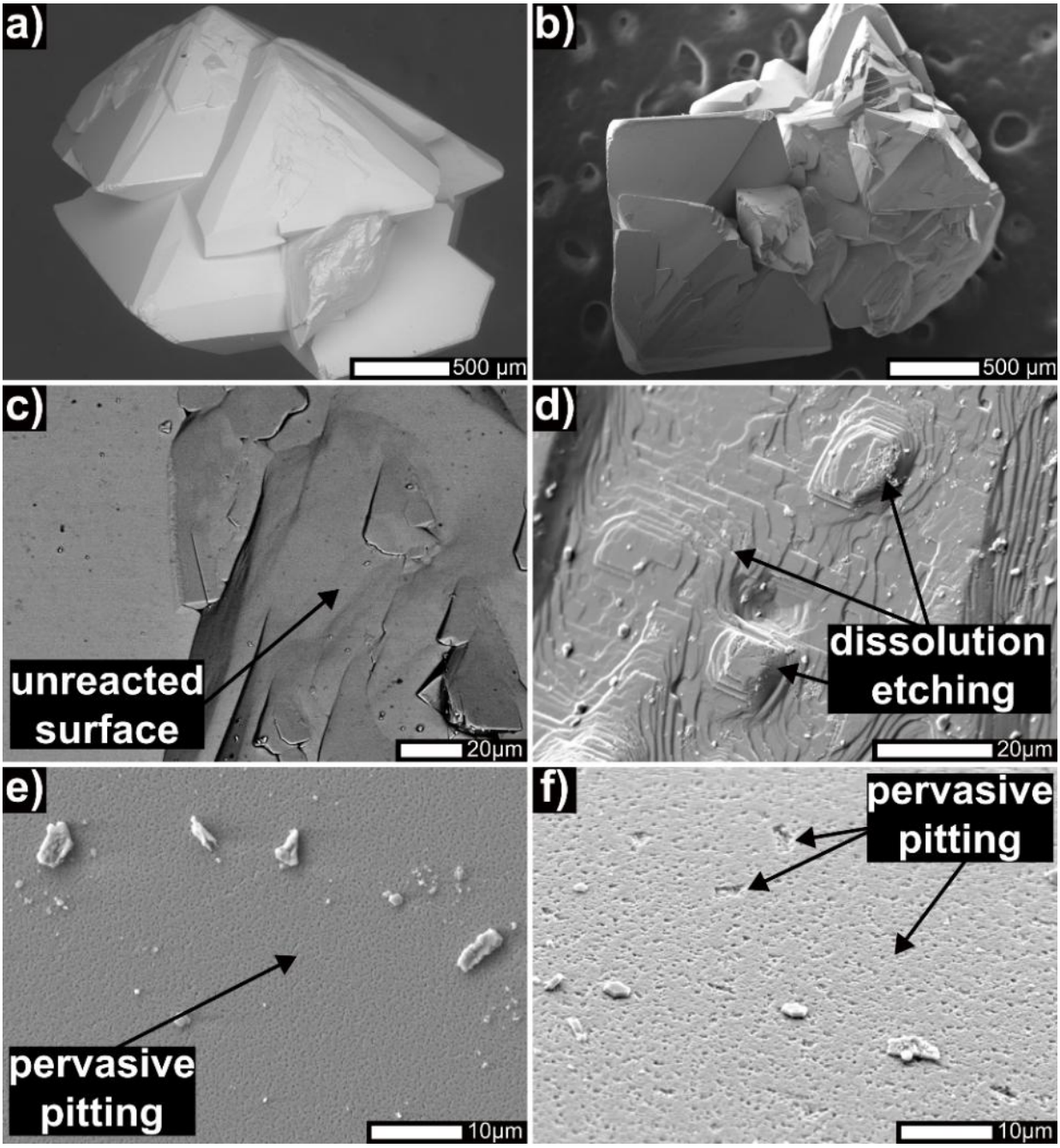

Figure 3. SEM images of unreacted (a) and reacted (b) $ErPO_4$ crystals. SEM high magnification images of c) an unreacted $ErPO_4$ crystal showing growth steps, d) a reacted crystal (starting pH 10) showing dissolution etching along growth steps and crystal edges, e) a magnified view of pervasive dissolution pits on a crystal reacted at starting pH 3, and f) pervasive dissolution pits on a crystal surface reacted at starting pH 2.

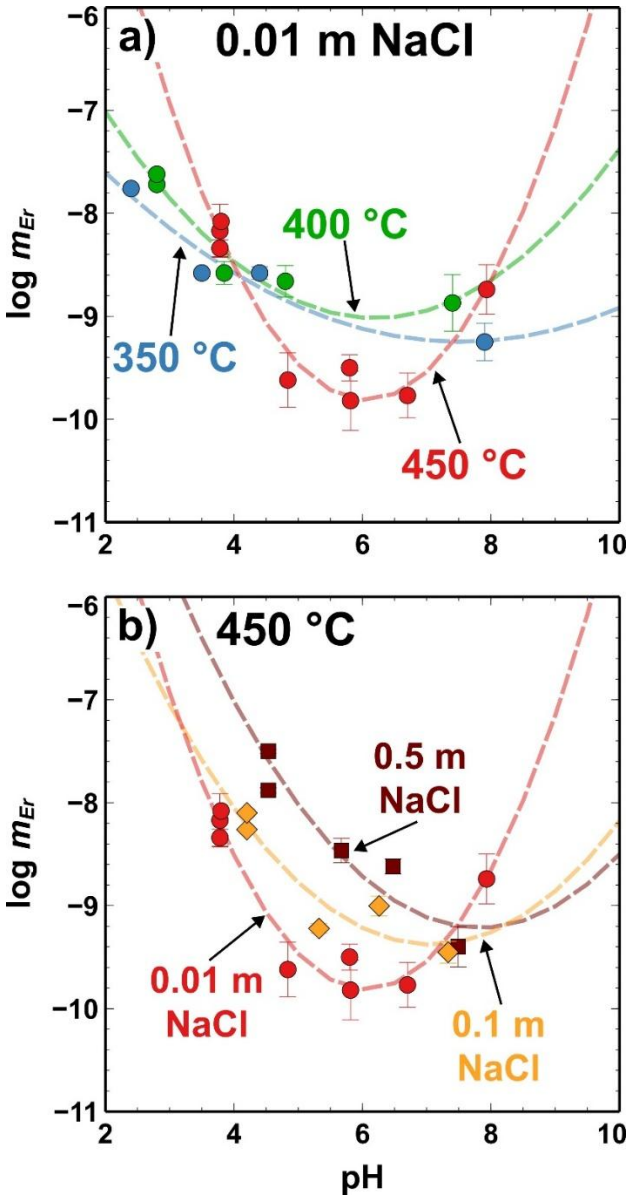

Figure 4. Erbium concentrations as a function of a) pH and temperature (350, 400, and 450 °C) at a constant salinity of 0.01 m NaCl and b) pH and salinity (0.01, 0.1, and 0.5 mol/kg NaCl) at a constant temperature of 450 °C. Curves are fitted using a quadratic polynomial of the second degree for better visualization of experimental data.

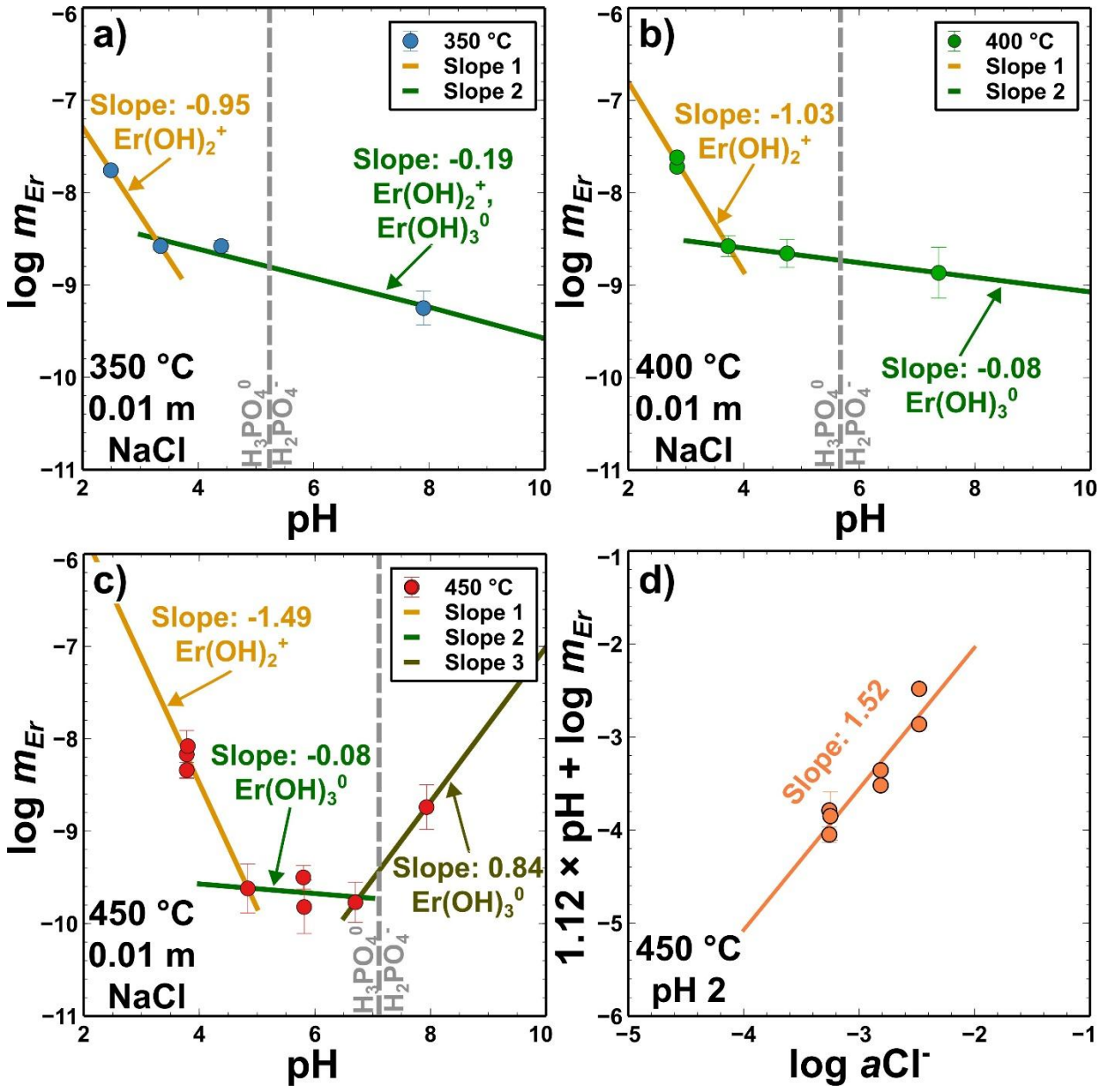

Figure 5. Experimental slope relationships used to estimate Er speciation as a function of logarithm of log m_{Er} and pH for experiments at 0.01 mol/kg NaCl and a) 350, b) 400, and c) 450 °C indicating the predominance of $ErOH_2^+$ and $ErOH_3^0$. The dominant phosphate species are shown by the grey dashed line and vary between pH ~5 at 350 °C and ~7.1 at 450 °C. d) At 450 °C, pH-corrected log m_{Er} show a slope of 1.52 with log a_{Cl^-} at a starting pH of 2, indicating the presence of $ErCl_2^+$ and $ErCl^{+2}$.

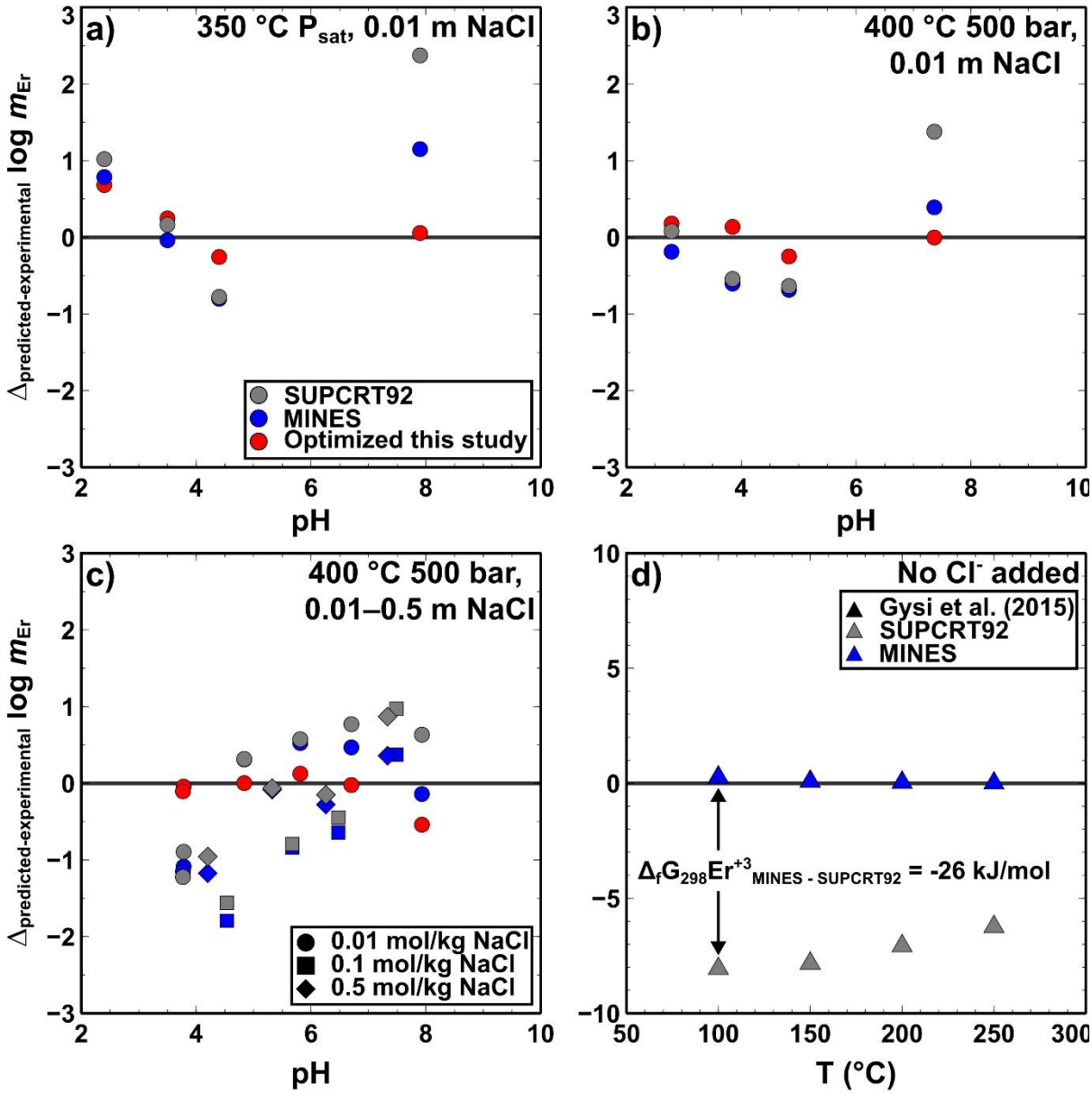

Figure 6. Difference $\Delta_{predicted-experimental}$ of predicted log m_{Er} (logarithm of molality dissolved Er) and experimentally measured $ErPO_4$ solubility showing experiments at a) 350 °C and 0.01 mol/kg NaCl, b) 400 °C and 0.01 mol/kg NaCl and c) 450 °C and 0.01, 0.1, and 0.5 mol/kg NaCl. $ErPO_4$ solubility was predicted using different thermodynamic datasets from SUPCRT92, MINES and optimized thermodynamic properties from this study. d) Measured $ErPO_4$ solubility in Gysi et al. (2015) is compared to predicted $ErPO_4$ solubility using the MINES and SUPCRT92 thermodynamic data sets. MINES shows excellent agreement at low pH (~2) in perchlorate solutions whereas SUPCRT92 shows discrepancies of up to 8 log units due to a -26 kJ/mol difference between the $\Delta_f G^0_{298}$ for Er^{+3} between the two databases. The sources of thermodynamic data are summarized in Table 2, and optimized thermodynamic data derived in this study are presented in Table 6.

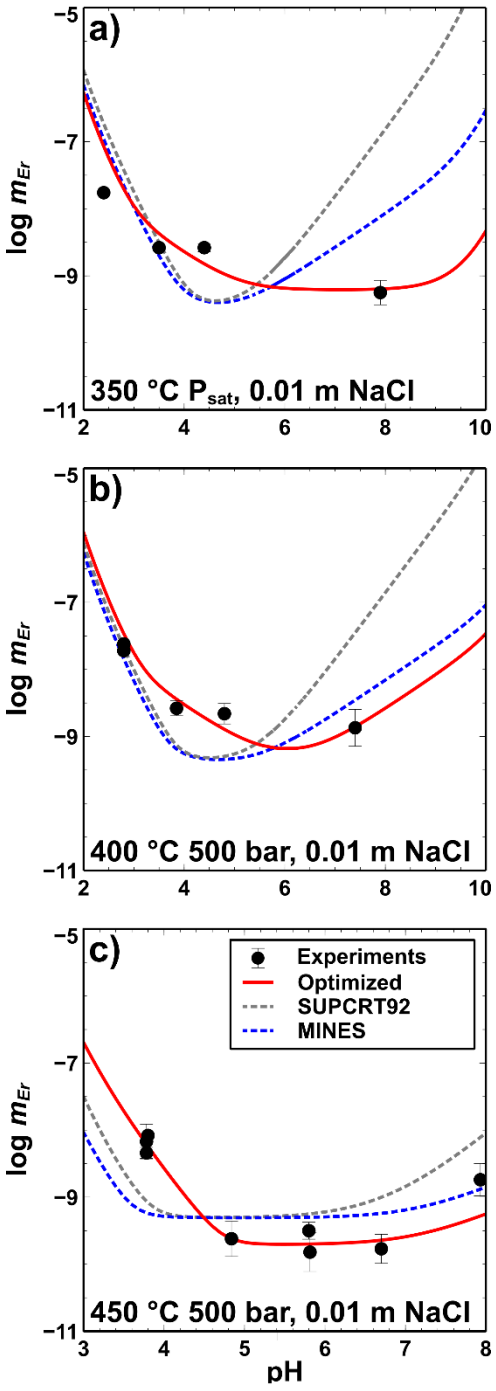

Figure 7. The predicted solubility of $ErPO_4$ as a function of pH at; a) 350, b) 400, and c) 450 °C and 0.01 mol/kg NaCl using thermodynamic properties for Er species from SUPCRT92, the MINES database, and the optimized data from this study. These modeling results using GEM-Selektor are also compared to the experimentally measured Er concentrations from Table 4.

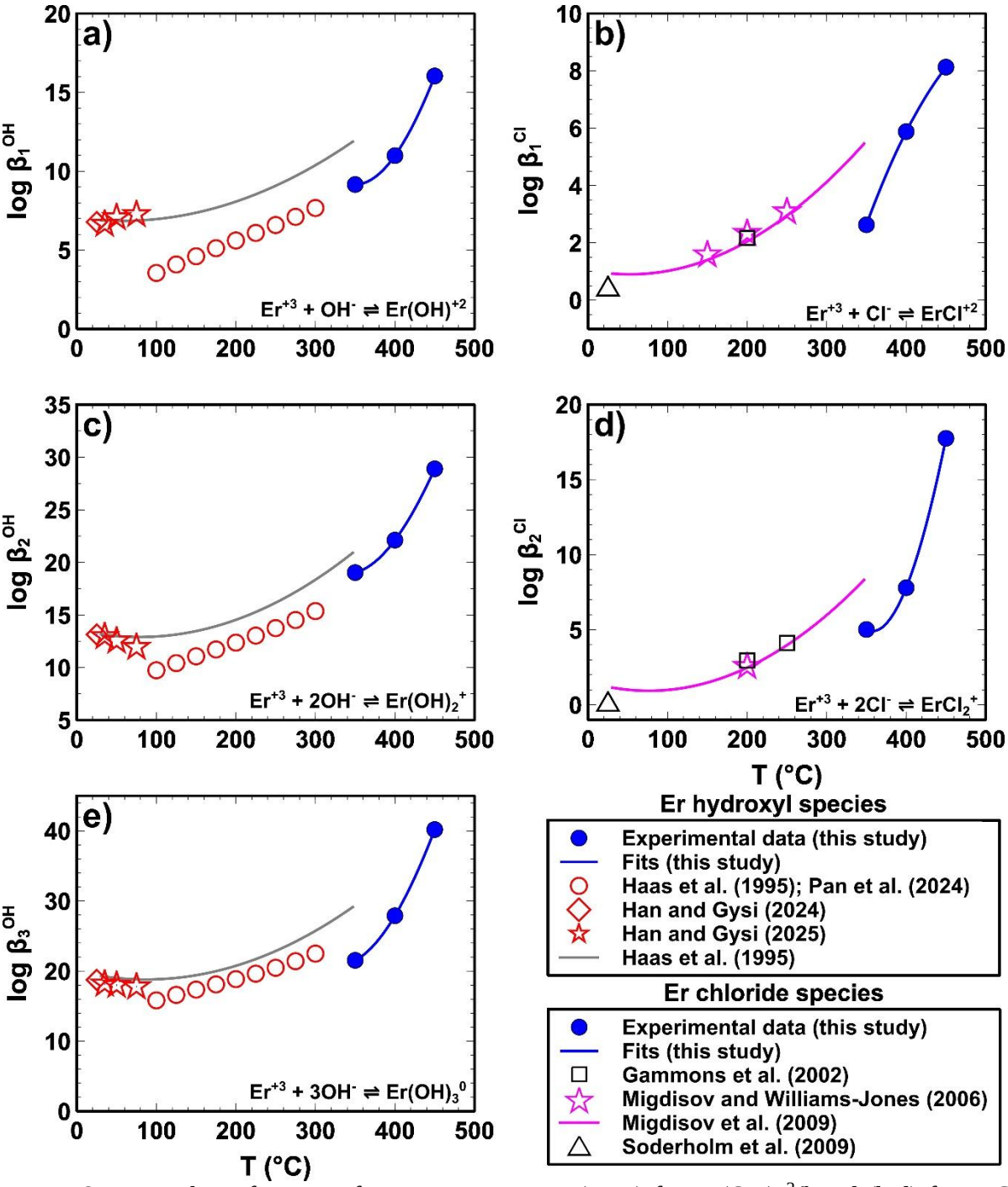

Figure 8. Logarithm of species formation constants (a,c,e) for $Er(OH)_n^{3-n}$ and (b,d) for $ErCl_n^{3-n}$ species derived from this study (Tables 7-8) compared to literature values at lower temperatures. Erbium hydroxyl data include those calculated from Haas et al. (1995) using the Er^{+3} aqua ion properties from Pan et al. (2024), those calculated from Haas et al. (1995) and SUPCRT92, and experimental UV-Vis data from Han and Gysi (2024; 2025). Erbium chloride data include experimental data from Gammons et al. (2002), Migdisov and Williams-Jones (2006), Migdisov et al. (2009), and Soderholm et al. (2009). The fits derived from experimental data from this study are calculated as a function of temperature from the coefficients listed in Table 7.

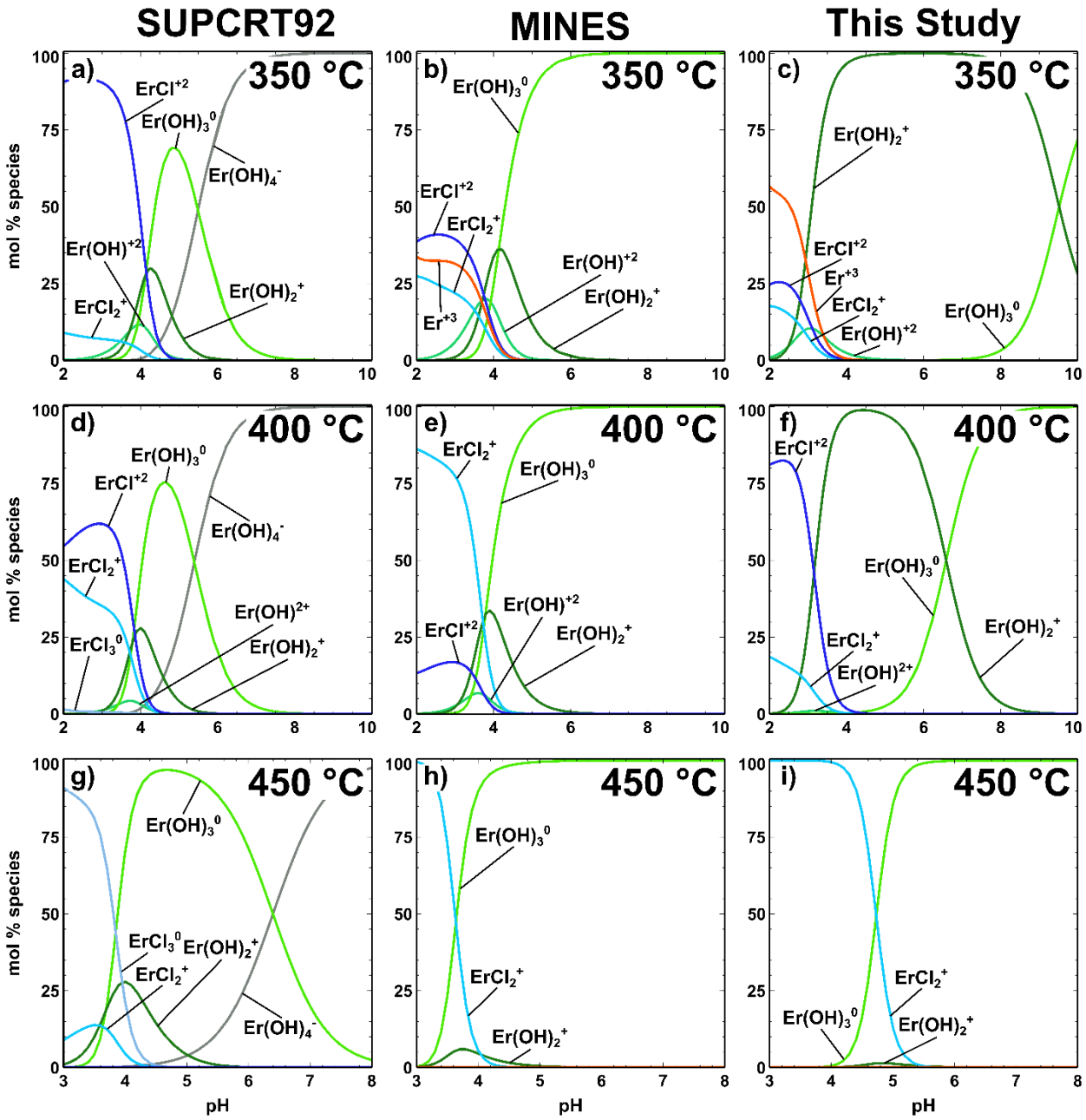

Figure 9. Predicted aqueous speciation (mol % species) as a function of pH at 350 °C and P_{sat} (a-c), 400 (d-f), and 450 °C (g-i) at 500 bar and 0.01 mol/kg NaCl using thermodynamic properties for Er species from SUPCRT92 (a,d,g), MINES database (b,e,h), and (c,f,i) the optimized data from this study (c,f,i). Comparison of these speciation calculations indicates significant differences with an increased stability of $Er(OH)_2^+$ and $Er(OH)_3^0$ in a wide pH range based on this study.

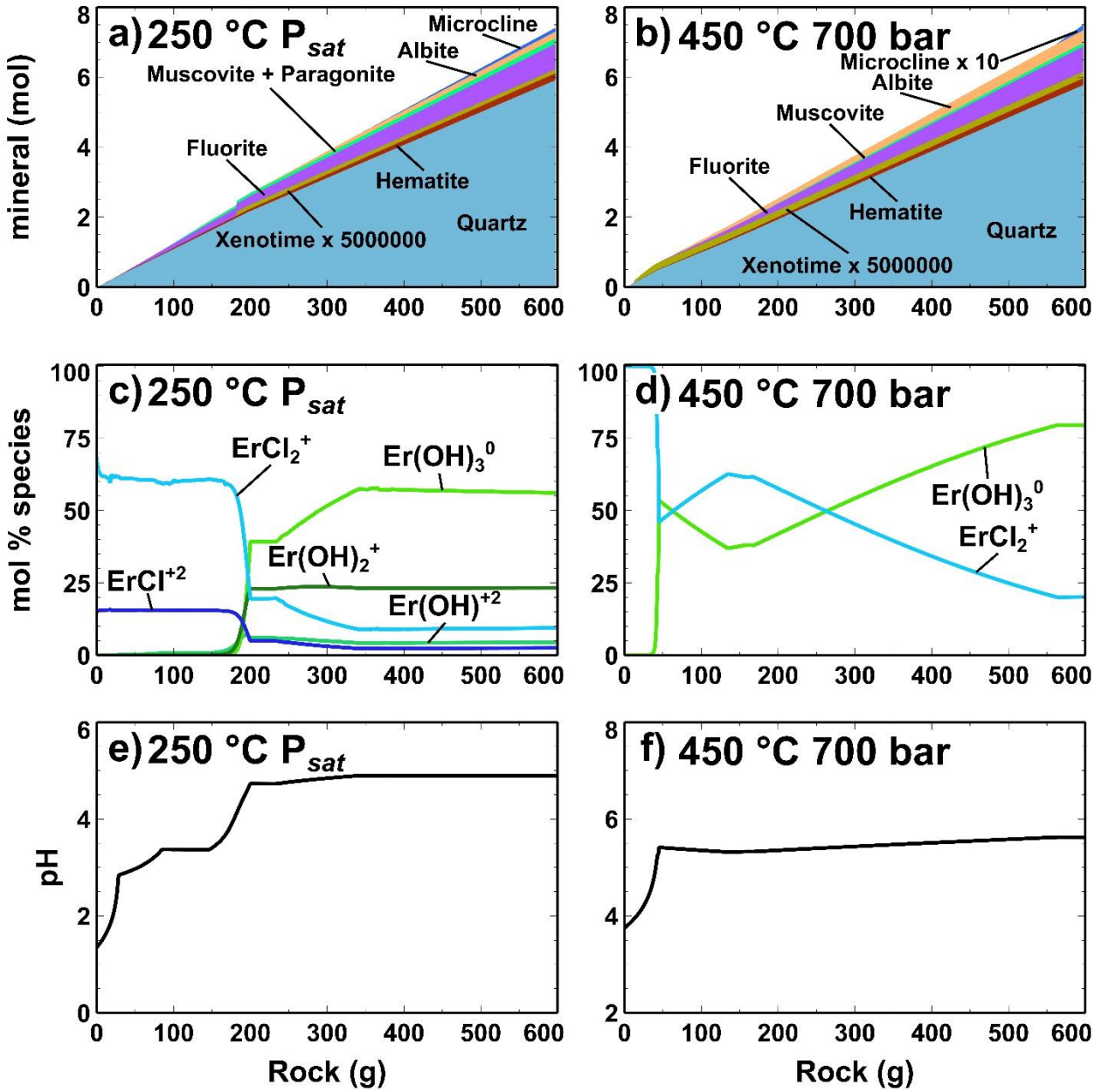

Figure 10. Rock titration simulation at (a, c, e) 250 °C and P_{sat} and (b, d, f) 450 °C and 700 bar as a function of pegmatite (g) added to 1 kg of acidic saline (5 wt.% NaCl, 0.1 M HCl) fluid. (a) The mineralogy at 250 °C changes from quartz- hematite-fluorite at fluid-buffered to quartz-hematite-muscovite-fluorite-albite-microcline at rock-buffered conditions. (b) The mineralogy at 450 °C shows comparable mineralogical zoning to the 250 °C model. (c-d) Relative abundance of Er species at 250 and 450 °C, respectively. (e-f) The pH increases from 1.3 to 4.7 at 250 °C and from 3.8 to 5.7 at 450 °C with increasing amounts of pegmatite, i.e., decreasing fluid to rock ratios.

TABLES

Table 1. Composition of the starting experimental solutions including pH, salinity, HCl/NaOH, and measured pH at room temperature.

Solution ID	NaCl (mol/kg)	pH	HCl (mol/kg)	NaOH (mol/kg)	Na[b] (mol/kg)
pH2-0.01 m NaCl	0.01	2.03	0.0135	-	0.0105
pH2-0.01 m NaCl	0.01	2.01	0.0129	-	0.0101
pH3-0.01 m NaCl	0.01	2.95	0.0010	-	0.0107
pH4-0.01 m NaCl	0.01	4.03	0.0001	-	0.0102
pH10-0.01 m NaCl[a]	0.01	10.48	-	0.0003	0.0104
pH10-0.01 m NaCl[a]	0.01	10.01	-	0.0001	0.0105
pH10-0.01 m NaCl[a]	0.01	10.29	-	0.0002	0.0101
pH10-0.01 m NaCl[c]	0.01	7.15	-	0.0001	0.0105
pH2-0.1 m NaCl	0.10	2.02	0.0135	-	0.1045
pH3-0.1 m NaCl	0.10	2.95	0.0010	-	0.1029
pH4-0.1 m NaCl	0.10	4.03	0.0001	-	0.1007
pH10-0.1 m NaCl[a]	0.10	10.10	-	0.0002	0.1002
pH2-0.5 m NaCl	0.50	2.03	0.0010	-	0.4969
pH3-0.5 m NaCl	0.51	2.95	0.0001	-	0.5179
pH4-0.5 m NaCl	0.50	4.03	0.0010	-	0.4932
pH10-0.5 m NaCl[a]	0.50	10.54	-	0.0006	0.4973

[a] pH-10 solutions are prepared on the day of the experiment.

[b] Measured using ICP-OES.

[c] Solution was prepared before the experiment using NaOH and pH measured on the day of experiment.

1105 Table 2. Thermodynamic data for aqueous species and solids considered in calculations and their
1106 sources.

Species/Mineral	**SUPCRT92** $\Delta_f G^0_{298}$ (kJ/mol)	**Ref.**	**MINES** $\Delta_f G^0_{298}$ (kJ/mol)	**Ref.**
Er^{+3}	-669	[1]	-695.2	[2]
$Er(OH)^{+2}$	-861.9	[4]	-861.9	[4]
ErO^{+} (e.g. $Er(OH)_2^{+}$)	-815.0	[4]	-841.2	[4]
ErO_2H^0 (e.g. $Er(OH)_3^0$)	-1004.6	[4]	-1004.6	[4]
ErO_2^- (e.g. $Er(OH)_4^-$)	-957.3	[4]	not included	
$ErCl^{+2}$	-802.1	[4]	-804.3	[3]
$ErCl_2^{+}$	-931.4	[4]	-934.2	[3]
$ErCl_3^0$	-1060.0	[4]	not included	
$ErPO_{4(s)}$	-1855.4 ± 2.1	[6,7,8]	-1855.4 ± 2.1	[6,7,8]
PO_4^{-3}, HPO_4^{-2}, $H_2PO_4^-$, $H_3PO_4^0$		[5]		[5]
H^+, OH^-		[5]		[5]
Cl^-		[5]		[5]
H_2O		[5]		[5]
Halite		[9]		[9]
$NaCl^0$, $NaOH^0$, Na^+		[10]		[10]
HCl^0		[11]		[11]

References: [1] Shock et al. (1997), [2] Pan et al. (2024), [3] Migdisov et al. (2009), [4] Haas et al. (1995), [5] SUPCRT92 (Johnson et al., 1992), slop98.dat database, [6] Gavrichev et al. (2012), [7] Ni et al. (1995), [8] Ushakov et al. (2001), [9] Robie and Hemingway (1995), [10] Miron et al. 2016, [11] Tagirov et al. (1997).

1107

1108

1109 Table 3. Conditions for GEMSFITS optimization.

GEMSFITS-Task	**Fitting mode**						**Optimized parameters**
	Er^{+3}	**$ErCl^{+2}$**	**$ErCl_2^{+}$**	**$ErOH^{+2}$**	**ErO^{+}**	**$ErOH_2^{0}$**	
Er-Cl species	S	F	F	S	S	S	$\Delta_f G^0_{298}$
Er-OH species	S	S_{Cl}	S_{Cl}	F	F	F	$\Delta_f G^0_{298}$

1110 Abbreviations: S: set/constant; F: fitted/optimized; S_{Cl}: not optimized and uses values from Er-Cl
1111 speciation task.

1112

Table 4. Experimental conditions including temperature (*T*), pressure (*P*), run time, starting pH at 25 °C Er, calculated pH at temperature and pressure and solution compositions.

T **°C**	**Time (days)**	***P*** **(bar)**	**$pH_{25°C}$** [a]	**pH_T** [b]	**NaCl (mol/kg)**	**Er (ppb)**	**1σ** [c] **(%)**	**log m_{Er}**
350	8	165	2.03	2.49	0.01	2.91	0.2	-7.76
350	8	165	2.95	3.35	0.01	0.44	0.4	-8.58
350	8	165	4.00	4.38	0.01	0.44	0.7	-8.58
350	8	165	10.48	7.93	0.01	0.09	2.0	-9.25
400	7	500	2.03	2.85	0.01	3.20	0.4	-7.72
400	7	500	2.03	2.85	0.01	4.04	0.2	-7.62
400	7	500	2.95	3.73	0.01	0.44	1.3	-8.58
400	7	500	4.00	4.75	0.01	0.37	1.8	-8.66
400	7	500	10.01	7.37	0.01	0.23	3.1	-8.87
450	9	500	2.01	3.83	0.01	0.77	1.0	-8.34
450	9	500	2.01	3.83	0.01	1.14	3.1	-8.17
450	9	500	2.95	4.79	0.01	0.04	2.7	-9.62
450	9	500	4.00	5.82	0.01	0.03	2.9	-9.82
450	9	500	10.29	7.93	0.01	0.30	2.8	-8.74
450	8	500	2.03	3.86	0.01	1.36	0.2	-8.08
450	8	500	4.00	5.76	0.01	0.05	1.3	-9.50
450	8	500	7.15	6.70	0.01	0.03	2.2	-9.77
450	8	500	2.03	4.23	0.10	0.92	0.2	-8.26
450	8	500	2.03	4.23	0.10	1.33	0.4	-8.10
450	8	500	2.95	5.21	0.10	0.10	0.5	-9.22
450	8	500	4.00	6.26	0.10	0.17	1.1	-9.00
450	8	500	10.10	7.33	0.10	0.06	1.1	-9.45
450	10	500	2.03	4.48	0.50	5.30	0.2	-7.50
450	10	500	2.03	4.48	0.50	2.20	0.3	-7.88
450	10	500	2.95	5.45	0.50	0.57	1.4	-8.47
450	10	500	4.00	6.39	0.50	0.40	0.8	-8.62
450	10	500	10.54	7.49	0.50	0.07	2.1	-9.40

[a] Initial pH measured at 25 °C before the experiment.

[b] pH at temperature and pressure calculated using GEM-Selektor.

[c] Propagated analytical error.

Table 5. Slope relationships of experimental $ErPO_4$ solubility data as a function of pH and log a_{Cl^-} expected Er species based on that slope.

Temperature °C	Salinity (mol/kg)	pH	Slope	Species	Intercept	R^2
pH: Er hydroxyl species						
350	0.01	2–4	-0.95	$ErOH_2^+$	-5.36	NA[a]
350	0.01	3–8	-0.19	$ErOH_3^0$	-7.98	0.92
400	0.01	2–4	-1.03	$ErOH_2^+$	-4.72	0.99
400	0.01	4–8	-0.08	$ErOH_3^0$	-8.28	1.00
450	0.01	4–5	-1.49	$ErOH_2^+$	-2.47	0.97
450	0.01	5–6	-0.08	$ErOH_3^0$	-9.20	0.19
450	0.01	7–8	0.84	$ErOH_3^0$	-15.38	NA[a]
450	0.1	4–5	-1.06	$ErOH_2^+$	-3.69	0.98
450	0.5	4–7	-0.54	$ErOH_3^0$	-5.29	0.93
450	0.01–0.5	4–5	-1.12	$ErCl_n^{3-n}$, $ErOH_2^+$	average	NA
log a_{Cl^-} - Er chloride species						
450	0.01–0.5	2	1.52	$ErCl^{+2}$, $ErCl_2^+$	1.00	0.90

[a] R^2 was not derived due to the slope being fit to two data points.

Table 6. Optimized standard Gibbs energy of formation ($\Delta_f G^0_{T,P}$) from GEMSFITS compared with thermodynamic data calculated from the MINES database and the composite scaled sensitivity (CSS) of each fitted species. Data for Er chloride are calculated from the HKF parameters derived in Migdisov et al. (2009) and data for Er hydroxyl species from Haas et al. (1995).

Temperature (°C)	Species	$\Delta_f G^0_{T,P}$ MINES (kJ mol $^{-1}$)	$\Delta_f G^0_{T,P}$ This Study (kJ mol $^{-1}$)	$\Delta_{opt\text{-}MINES}$[a] (kJ mol $^{-1}$)	CSS
350	$ErCl^{+2}$	-804.3[c]	-799.3	5.0	0.6
	$ErCl_2^{+}$	-934.2[c]	-929.2	5.0	0.5
	$Er(OH)^{+2}$	-861.9[d]	-865.2	-3.3	0.2
	ErO^{+} [b]	-815.0[d]	-834.1	-19.0	4.0
	ErO_2H^0 [b]	-1004.6[d]	-960.0	44.6	0.02
400	$ErCl^{+2}$	-804.3[c]	-822.2	-17.9	3.0
	$ErCl_2^{+}$	-934.2[c]	-933.4	0.8	0.5
	$Er(OH)^{+2}$	-861.9[d]	-866.9	-4.9	0.04
	ErO^{+} [b]	-815.0[d]	-840.1	-25.1	2.8
	ErO_2H^0 [b]	-1004.6[d]	-993.6	11.0	1.2
450	$ErCl^{+2}$	-804.3[c]	-804.4	-0.1	0.01
	$ErCl_2^{+}$	-934.2[c]	-971.3	-37.1	2.9
	$Er(OH)^{+2}$	-861.9[d]	-864.5	-2.6	0.01
	ErO^{+} [b]	-815.0[d]	-810.4	4.6	0.03
	ErO_2H^0 [b]	-1004.6[d]	-993.4	11.1	3.5

[a] $\Delta_f G^0_{T,P}$ in the MINES thermodynamic database - optimized $\Delta_f G^0_{T,P}$ this study.

[b] $\Delta_f G^0_{T,P}$ values can be converted to hydrous formula using the $\Delta_f G^0_{T,P}$ values of H_2O at P-T, according to: ErO^+ [$+H_2O = Er(OH)_2^+$] and ErO_2H^0 [$+H_2O = Er(OH)_3^0$]. [c] Value derived from Migdisov et al. (2009). [d] Value derived from Haas et al. (1995).

Table 7. Logarithmic $\beta_n^{(Cl,OH)}$ cumulative formation constants for Er species optimized in this study.

T (°C)	$Log\beta_1^{OH}$	$Log\beta_2^{OH}$	$Log\beta_3^{OH}$	$Log\beta_1^{Cl}$	$Log\beta_2^{Cl}$
350	9.16	19.03	21.53	2.63	5.02
400	10.99	22.12	27.9	5.88	7.8
450	16.04	28.9	40.19	8.13	17.75

Table 8. Regressed coefficients (A_0-A_2) for the logarithm of cumulative formation constant using the equation; $\log\beta_n^{(Cl,OH)} = A_0 + A_1 t + A_2 t^{-1}$ with t in Kelvin and standard enthalpy of formation for aqueous Er chloride and hydroxyl complexes based on experiments and optimizations conducted in this study for conditions between 350 °C at P_{sat} and 400–450 °C at 500 bar.

Species	A_0 x10^2	A_1 x10^{-2}	A_2 x10^4	$\Delta_f H_{Tr,Pr}^0$ (kJ mol $^{-1}$)
$ErCl^{+2}$ ($\log\beta_1^{Cl}$)	1.496	-7.963	-6.067	1025.9
$ErCl_2^+$ ($\log\beta_2^{Cl}$)	-13.74	109.2	43.50	-6468.0
$Er(OH)^{+2}$ ($\log\beta_1^{OH}$)	-6.173	50.23	19.54	-2884.9
$Er(OH)_2^+$ ($\log\beta_2^{OH}$)	-7.113	59.55	22.39	-3272.2
$Er(OH)_3^0$ ($\log\beta_3^{OH}$)	-11.68	98.36	35.92	-5201.7

SUPPLEMENTARY MATERIAL

The supplementary documents included here and additional information on Er extraction and the H_2SO_4-washing technique developed in this study, Table S1. A summary of all wash techniques and the efficiency of each wash, and Table S2. Raman peak positions for unreacted and reacted solids. Supplemental Tables S1-S14 and main Tables 1 – 7 are provided in a separate excel document which is appended as Data availability doi: 10.17632/r6r429f223.1

Tables in the excel document include:

- Table S1: H_2SO_4 washing technique summary table highlighting the three wash techniques used throughout the study.
- Table S2: Raman peak positions of reacted and unreacted $ErPO_4$ crystals compared with values from Hurtig et al. (2024).
- Table S3: Supplementary table for Raman Peak positions as shown in Figure 2.
- Table S4. Supplementary table for $ErPO_4$ Experimental data from this study which is used in Figures 4, 5, and 7.
- Table S5. Supplementary table for lines of fit for experimental data as shown in Figure 4.
- Table S6. Supplementary table for solubility slopes as shown in Figure 5.
- Table S7. Supplementary table for Figure 6. Comparison between SUPCRT92 and Mines thermodynamic databases and optimized data in this study with experimental solubility results expressed as log difference for 350, 400, and 450 C at 0.01 mol/kg NaCl. Experiments at higher salinities of 0.1 and 0.5 mol/kg NaCl are also compared. Experimental data from Gysi et al. (2015) is compared to calculations by the MINES and SUPCRT92 databases to show consistency with previous experimental studies.
- Table S8. Supplementary table for Figure 6. Logβ formation constants for each species from literature data.
- Table S9. Supplementary table for Figure 6. Logβ formation constants for each species optimized in this study and their lines of fit.
- Table S10. Supplementary table for Figures 7 and 9 showing SUPCRT92 models of Er solubility and speciation (in log mol/kg) at 350, 400, and 450 °C and 0.01m NaCl.
- Table S11. Supplementary table for Figures 7 and 9 showing MINES thermodynamic database models of Er solubility and speciation (in log mol/kg) at 350, 400, and 450 °C and 0.01m NaCl.
- Table S12. Supplementary table for Figures 7 and 9 showing models of Er solubility and speciation (in log mol/kg) at 350, 400, and 450 °C and 0.01m NaCl that using thermodynamic data for species optimized in this study.
- Table S13. Supplementary table for Figure 10 for a rock titration simulation conducted in GEM-Selektor at 250 °C and Psat and 450 °C and 700 bar as a function of pegmatite (g) added to 1 kg of acidic saline (5 wt.% NaCl, 0.1 M HCl) fluid. Mineral concentrations are shown in moles of mineral and aqueous Er species are shown in log mol/kg.
- Table S14. Parameters used for the calculation of solution density at experimental conditions using the SoWat code package based on Driesner and Heinrich (2007).

H_2SO_4-washing technique for extraction of Er from $ErPO_4$ solubility experiments

Precipitation of REE solids upon quenching is a common issue in Cl-bearing solutions, specifically in hydrothermal experiments conducted at elevated temperatures (Migdisov et al., 2009; Banerjee et al., 2025). At temperatures of 150 to 250 °C Migdisov et al. (2009) reports the precipitation of secondary $REEF_3$ during quenching and uses multiple washes of 5 ml of concentrated H_2SO_4 in order to successfully remove the precipitates. At high temperatures of 500 to 700 °C, $NdPO_4$ precipitation was so severe that an isotope dilution method needed to be used, as even prolonged leaching in concentrated H_2SO_4 could not redissolve all the precipitated material (Banerjee et al., 2025).

Solubility experiments required multiple washes of each autoclave due to precipitation of Er on the walls of the autoclaves upon quenching. Three styles of wash techniques were used within this study, of which, data from wash techniques 2 and 3 were used in thermodynamic calculations. Based on Migdisov et al. (2009), wash technique 1 was employed first, which included three separate "cold" washes using ~4 ml of concentrated sulfuric acid H_2SO_4 at ambient temperatures (Fig. S1a). These washes produced Er concentrations of -9.8 to -10.5 log mol/kg Er (Table S1). Experimental fluid and wash contributions to overall Er averaged 74 % for experimental fluid, 9 % for wash 1 and 8 % for washes 2 and 3.

To test the efficiency of wash technique 1, a "hot wash" using a 1 % H_2SO_4 solution at ~160 °C for 4 days was used (wash technique 2) during experiments at 450 °C. The "hot wash" accounted for ~90 % of all Er extracted from the experiment whereas experimental fluid totaled 8 % of all Er and cold washes only accounted for 1% of total Er respectively (Table S1, Fig. S1a).

To expand upon this method and ensure all Er was being successfully extracted, a final wash technique 3 was implemented where two hot washes are conducted followed by a final cold wash. The results of wash technique 3 saw systematic diminishing returns with washes one, two and three returning an average of 71 % (hot), 22 % (hot), and 2 % (cold) of measured Er with the experimental fluid contributing to 5% overall solubility (Table S1, Fig. S1a). At pH 2, these totals are 6 % for experimental fluid, 77 % for wash 1, 16 % for wash 2, and 1 % for wash 3; at pH 3 these totals are 2 % for experimental fluid, 76 % for wash 1, 19 % for wash 2, and 3 % for wash 3; at pH 4 these totals are 2 % for experimental fluid, 67 % for wash 1, 25 % for wash 2, and 6 % for wash 3; finally, at pH 10 these totals are 8 % for experimental fluid, 55 % for wash 1, 36 % for wash 2, and 1 % for wash 3 (Table S1). These results show a decrease in wash efficiency with increasing pH as a steadily higher proportion of Er is extracted from wash 2. This, however, is likely a result of the generally lower concentrations of Er within more alkaline experiments. The wash technique 3 was the most effective method and removes all Er precipitated onto the walls of reactors. The effectiveness of wash technique 3 is further supported by the consistency in Er

concentration for replicates and solubility results over the course of multiple experiments (Table S1, Fig S1b).

To ensure that the wash technique extracted all precipitated Er and reduce the impact of

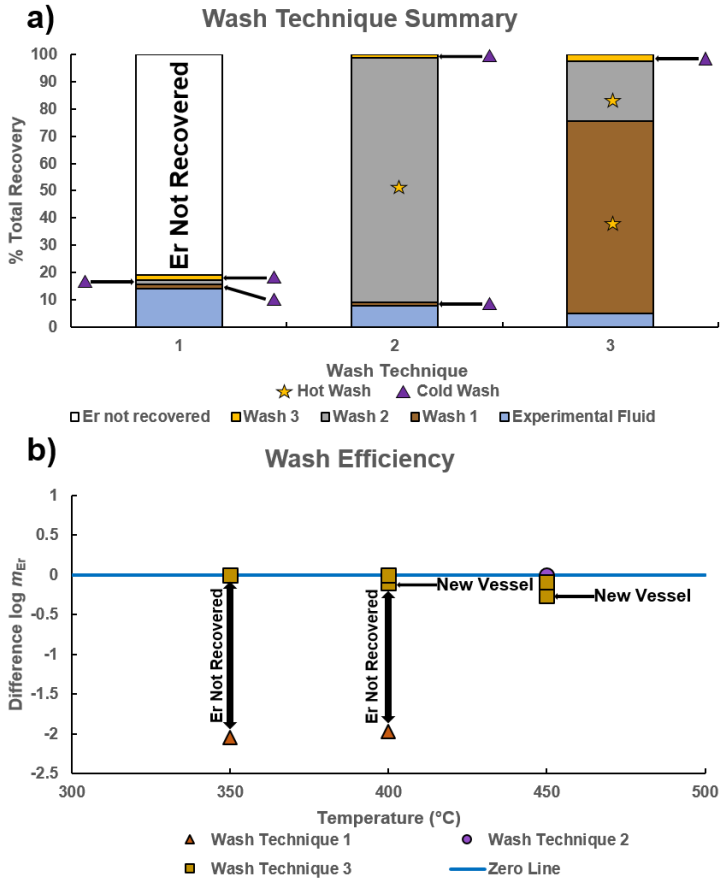

Figure S1. Comparison of three different wash techniques, showing a) contribution of extracted Er in individual steps of the washing technique and b) wash efficiency in comparison to the highest Er value, as well as different duplicate experiments that have undergone different washing steps. a) Wash technique 1 included the experimental solution, and three consecutive cold concentrated H_2SO_4 washes similar to the method employed in Migdisov et al. (2009). Wash technique 2 included the experimental solution, a cold concentrated H_2SO_4 wash followed by a hot wash using 1% H_2SO_4 and another cold concentrated H_2SO_4 wash. Wash technique 3 included two consecutive hot washes using 1% H_2SO_4 and one cold concentrated H_2SO_4 wash at the end. b) The efficiency of each wash technique is shown as a logarithm of mol/kg difference between the highest concentration starting pH 2 experiment (zero line) and each starting pH 2 experimental Er concentration from this study as a function of temperature, including a new and unused reactor which has Er values within experimental error. The different wash techniques are denoted.

carry over between experiments, duplicate experiments were conducted in a new experimental vessel which had no prior contact with $ErPO_4$ (Table S1). The analyzed results are well within experimental error (5%) of vessels used in previous Er bearing solubility experiments.

Furthermore, the experimental series conducted using wash technique 2 was also within experimental error of those using wash technique 3 and was therefore included in Er speciation calculations (Fig S1b). The experimental totals for Er using wash technique 1 are almost two orders of magnitude lower than what was recovered using wash techniques 2 and 3 (Fig. S1b) and were therefore excluded from the study altogether (Table S1, Fig. S1b).

Table S1: H_2SO_4 washing technique summary table highlighting the three wash techniques used throughout the study.

Temperature °C	pH 25 °C	NaCl mol/kg	Er conc. log mol/kg	Exp. Fluid	Wash 1 %	Wash 2	Wash 3	Wash Technique
350[a]	2	0.01	-9.82	90.3	3.6	3.2	2.9	1
350[a]	3	0.01	-10.30	72.9	9.6	8.5	9.0	1
350[a]	4	0.01	-10.45	63.7	11.8	11.6	12.9	1
350[a]	10	0.01	-10.42	63.0	12.3	12.2	12.4	1
350	2	0.01	-7.76	2.0	88.0	9.3	0.8	3
350	3	0.01	-8.58	1.4	87.2	10.3	1.1	3
350	4	0.01	-8.58	1.2	79.5	16.3	3.0	3
350	10	0.01	-9.25	2.9	54.1	40.1	2.9	3
400[a]	2	0.01	-9.59	95.0	1.9	1.7	1.4	1
400[a]	3	0.01	-10.41	70.9	10.6	9.1	9.4	1
400[a]	4	0.01	-10.48	68.9	10.8	10.1	10.2	1
400[a]	10	0.01	-10.50	70.7	9.8	10.0	9.4	1
400[b]	2	0.01	-7.72	0.4	91.0	8.4	0.2	3
400	2	0.01	-7.62	1.7	89.7	8.1	0.5	3
400	3	0.01	-8.58	2.1	65.1	32.0	0.8	3
400	4	0.01	-8.66	0.2	51.9	46.9	1.1	3
400	10	0.01	-8.87	0.6	30.3	68.0	1.1	3
450	2	0.01	-8.08	7.1	0.1	92.7	0.1	2
450	4	0.01	-9.5	7.6	1.5	89.4	1.5	2
450	10	0.01	-9.77	15.5	2.8	79.0	2.8	2
450[b]	2	0.01	-8.34	0.4	91.0	8.4	0.2	3
450	2	0.01	-8.17	14.3	65.0	19.6	1.1	3
450	3	0.01	-9.62	2.5	66.2	20.7	10.6	3
450	4	0.01	-9.82	1.8	41.6	40.4	16.3	3
450	10	0.01	-8.74	0.4	69.9	28.3	1.4	3
450[b]	2	0.10	-8.26	6.1	72.4	20.6	0.9	3
450	2	0.10	-8.1	8.5	70.4	20.7	0.4	3
450	3	0.10	-9.22	0.2	82.3	16.1	1.4	3
450	4	0.10	-9	3.1	83.7	11.6	1.6	3
450	10	0.10	-9.45	12.3	66.7	19.6	1.4	3
450[b]	2	0.50	-7.5	2.9	77.6	18.9	0.6	3
450	2	0.50	-7.88	5.3	73.2	20.8	0.7	3
450	3	0.50	-8.47	2.7	79.0	17.3	1.0	3
450	4	0.50	-8.62	3.4	78.4	8.9	9.4	3
450	10	0.50	-9.4	23.0	53.1	23.9	0.0	3

[a] Experiments conducted using wash technique 1 which were not used in the manuscript due to low Er concentrations which we do not believe to be representative of the true concentrations of Er.
[b] Replicate experiments conducted with an autoclave only used during wash technique 3.

Raman spectra for $ErPO_4$ solids

The $ErPO_4$ solids used in this study were analyzed using Raman spectroscopy to ensure that the purity of the phase was maintained and was not altered to a hydrated REE phase (i.e. rhabdophane, churchite, and Er-hydroxides). The v_1 and v_3 PO_4^{-3} tetrahedron stretching vibrations from crystals used in experiments are shown in Table S1 and are compared to analyses of unreacted $ErPO_4$ crystals from both this study and Hurtig et al. (2024). The reacted crystal v_1- and v_3-PO_4 peak centers are within uncertainty of both the analyses of unreacted crystals from this study and Hurtig et al. (2024). No additional peaks were detected that indicate a secondary Er-bearing phase.

Table S2. Raman peak positions of reacted and unreacted $ErPO_4$ crystals compared with values from Hurtig et al. (2024).

Starting pH	v_1-PO_4 (cm^{-1})		v_3-PO_4 (cm^{-1})	
	Center	FWHM	Center	FWHM
2	1002.3	2.0	1059.1	2.7
2	1002.2	1.5	1059.1	2.3
3	1001.6	2.1	1058.6	3.4
4	1001.9	1.7	1058.9	2.6
10	1002.2	2.0	1059.1	2.7
Unreacted	1002.4	1.5	1059.3	2.1
Hurtig et al. (2024)	1002±0.5		1059±0.5	